

RESEARCH ARTICLE

10.1002/2014JB011145

Key Points:

- The central Basin and Range undergoes active crustal deformation
- Deformation is shear, suggesting that the Pacific Plate drives relative motion
- Deformation is inconsistent with an active megadetachment

Correspondence to:

W. C. Hammond,
whammond@unr.edu

Citation:

Hammond, W. C., G. Blewitt, and C. Kreemer (2014), Steady contemporary deformation of the central Basin and Range Province, western United States, *J. Geophys. Res. Solid Earth*, 119, doi:10.1002/2014JB011145.

Received 21 MAR 2014

Accepted 2 JUN 2014

Accepted article online 4 JUN 2014

Steady contemporary deformation of the central Basin and Range Province, western United States

William C. Hammond¹, Geoffrey Blewitt¹, and Corné Kreemer¹

¹Nevada Geodetic Laboratory, Nevada Bureau of Mines and Geology, and Nevada Seismological Laboratory, University of Nevada, Reno, Nevada, USA

Abstract We use data from western U.S. GPS networks to estimate the rate, pattern, and style of tectonic deformation of the central Basin and Range Province (BRP). Previous geodetic investigations have found the crust of eastern Nevada and western Utah to act as a rigid microplate, with zero deformation rates to within measurement uncertainty. Observed transients in GPS time series have led others to propose a megadetachment model, predicting that the central BRP behaves as a microplate, but with time-varying translation. Here we reassess these hypotheses, benefiting from a significant increase in GPS stations and time span, and innovations in analysis techniques. Our results show that the BRP crust deforms everywhere and all the time. In a group of 24 stations between longitude -113.5° and -116.8° , we find strain rates of $1.9 \pm 0.2 \times 10^{-9} \text{ yr}^{-1}$ extension directed N55°W and $2.2 \pm 0.2 \times 10^{-9} \text{ yr}^{-1}$ contraction directed N35°E, inconsistent with microplate behavior. The linearity of time series of strain from GPS station triplets is inconsistent with episodic translation of quasi-rigid domains. One exception is station EGAN that exhibits nonlinear motion not found in adjacent stations. The dominant signal in Nevada is distributed shear consistent with Pacific/North America relative plate motion, suggesting that stresses are transmitted through the lithosphere at least 800 km from the plate boundary. The observed active extension is consistent with earthquake focal mechanisms and is in agreement with integrated rates estimated from earthquake geology. Our results do not support the proposed megadetachment in the BRP.

1. Introduction

Debate over the rates, modes, and mechanisms of tectonic deformation of continental interiors has endured since the first studies of active crustal deformation in plate boundary zones. In the Basin and Range Province (BRP), western United States, such fundamental questions as whether the deformation is inherently block-like or fluid-like, steady or episodic, have been difficult to answer [England and McKenzie, 1982; Thatcher, 2009]. The debate has been fueled by our desire to understand the fundamental forces that drive tectonic deformation and by the need to document the distribution of earthquake potential in a way that best prepares society from damaging earthquakes. New geodetic networks, such as the EarthScope Plate Boundary Observatory (<http://pbo.unavco.org>), are now providing decade or longer records at a greater number of locations, which are needed to resolve patterns of slow crustal deformation in plate boundary interiors.

In the BRP, most of the active deformation occurs near the perimeters of the province. The Walker Lane to the west experiences $\sim 10 \text{ mm yr}^{-1}$ of transtension [e.g., Dokka and Travis, 1990; Bennett et al., 1998; Thatcher et al., 1999; Wernicke et al., 2000; Dixon et al., 2000; Miller et al., 2001; Oldow et al., 2001; McClusky et al., 2001; Hammond and Thatcher, 2004], while in the eastern BRP, near the Wasatch fault zone, extension occurs at $3\text{--}4 \text{ mm yr}^{-1}$ [Martinez et al., 1998; Niemi et al., 2004; Chang et al., 2006; Puskas and Smith, 2009; Kreemer et al., 2010].

Between these peripheral zones, previous geodetic investigations have found the crust acting as a microplate, with zero deformation rates to within measurement uncertainty [e.g., Bennett et al., 2003; Hammond and Thatcher, 2004; Kreemer et al., 2010]. However, some authors have maintained that broadly distributed deformation occurs across some of, if not the entire, province and is detectable in the GPS data [e.g., Wernicke et al., 2000; Puskas and Smith, 2009; Payne et al., 2012; Petersen et al., 2014]. Diffuse microseismicity in addition to occasional larger earthquakes such as the 2008 Wells, NV, M_w 6.0 event [dePollo et al., 2011], the presence of the large numbers of geologically young earthquake surface ruptures [dePollo, 2008], and neotectonic studies [e.g., Wesnousky et al., 2005; Koehler and Wesnousky, 2011] support the view that tectonic deformation is ongoing between the zones of peripheral deformation.

Here we use new GPS observations to show that all regions as large as the spacing of long-running GPS stations in the BRP (typically ~100 km) in eastern Nevada and western Utah are undergoing measurable active tectonic deformation. This has implications for the mode of deformation, source of the driving stress, the budget of deformation available between the BRP and the Sierra Nevada, and for the distribution of seismic hazard in the Intermountain West. We find that shear deformation dominates over uniaxial extension despite the clear geologic record of west-northwest-directed extension on north-northeast-striking normal faults. The style of geodetically measured deformation is similar to the orientation of the more rapidly deforming Walker Lane Belt, where a similar mismatch between geologically recorded extensional strain release and geodetic shear strain accumulation is documented across en echelon basins [Wesnousky *et al.*, 2012]. The persistence of this shear extension mismatch across the BRP suggests a common mechanism (or bias) in the comparison of geologic to geodetic data and has broad implications for reconciling short-term geodetic measurements with long-term estimates of crustal deformation.

2. GPS Data and Analysis

2.1. Analysis of GPS Data

GPS data were collected in the networks of the Basin and Range Geodetic Network (BARGEN), Eastern Basin and Range-Yellowstone (EBRY) network, EarthScope Plate Boundary Observatory (PBO), and Mobile Array of GPS for Nevada Transtension (MAGNET) network (Table 1 and Figure 1). We analyze all available GPS data from 1996 to January 2013 from the UNAVCO, Inc. or Scripps Orbit and Permanent Array Center (SOPAC) archives in RINEX format. The earliest usable data come from the BARGEN stations that began collecting data in July 1996 [Bennett *et al.*, 1998; Wernicke *et al.*, 2000]. Each network is operated continuously except for MAGNET that is operated in semicontinuous mode [Blewitt *et al.*, 2009; Hammond *et al.*, 2011a]. This analysis includes only two EBRY stations because most stations in that network lie east of 112°W longitude. The station CEDA has collected data for 16.5 years, having the longest duration in our analysis.

The data were processed as a part of a >12,000 station mega network analysis system that retrieves data daily and updates solutions weekly. We use the GIPSY/OASIS software provided by the Jet Propulsion Laboratory (JPL) to estimate station coordinates every 24 h using the precise point positioning method [Zumberge *et al.*, 1997]. Ionosphere-free combinations of carrier phase and pseudorange were obtained every 5 min. Calibrations were applied for all antennas, ground receivers, and satellite transmitters. To model tropospheric refractivity, the Global Mapping Function was applied [Boehm *et al.*, 2006], with tropospheric wet zenith delay and horizontal gradients estimated as stochastic random walk parameters every 5 min [Bar Sever *et al.*, 1998]. The observable model includes ocean tidal loading (including companion tides) coefficients supplied by Chalmers University [Scherneck, 1991]. Ambiguity resolution was applied to double differences of the estimated one-way bias parameters [Blewitt, 1989], using the wide lane and phase bias methods, which phase connects individual stations to International Global Navigation Satellite Systems Service (IGS) stations in common view [Bertiger *et al.*, 2010]. Satellite orbit and clock parameters were provided by the JPL, who determine these parameters in a global fiducial-free analysis using a subset of the available IGS core stations as tracking sites.

Output station coordinates are initially in the loose frame of JPL's fiducial-free GPS orbits. Finally, the solutions are aligned by seven parameter transformation (for each day) with our custom reference frame (NA12) that corotates with stable North America [Blewitt *et al.*, 2013]. These daily transformations are publicly available at <ftp://gneiss.nbmj.unr.edu/x-files>, and the solutions are available at <http://geodesy.unr.edu>. This alignment provides a spatial filter to suppress errors correlated at the continental scale.

We deleted positions that were immediately recognizable outliers in the time series, i.e., those with values more than 20 mm from the expected position for each site based on a provisional linear model of the time series, or positions with uncertainties in any coordinate greater than 20 mm. The mean formal uncertainty in daily coordinates is 0.6 and 0.5 in the north and east directions, respectively. The actual daily scatter of detrended time series in NA12 has a root-mean-square (RMS) of 1.0 mm in the north and 0.9 mm in the east. We only used stations that had at least 2.5 years of data. The resulting east, north, up time series are used to estimate rates of motion with respect to stable North America (Figure 1).

Table 1. Velocities of GPS Stations in NA12 Reference Frame

Station Name	Latitude	Longitude	Vn	Ve	Svn	Sve	Network	Day of First Data
ALAM	37.358	-115.1585	-0.22	-2.66	0.05	0.05	BARGEN	13 Jun 1999
ANTB	39.8479	-117.3709	0.35	-3.06	0.05	0.07	MAGNET	9 Sep 2004
BAMO	40.4128	-117.2046	0.04	-2.98	0.04	0.04	BARGEN	2 Feb 2003
BATT	40.5159	-117.2089	-0.59	-2.89	0.16	0.09	MAGNET	9 Sep 2004
BEAT	37.0399	-116.6211	0.43	-2.89	0.05	0.03	BARGEN	20 Jan 1999
BEE5	39.2672	-117.7095	0.23	-3.26	0.06	0.08	MAGNET	7 Sep 2006
BIG5	39.286	-116.8249	0.30	-2.85	0.31	0.56	MAGNET	18 Oct 2007
BOBS	39.448	-116.982	-0.08	-2.44	0.09	0.64	MAGNET	18 Oct 2007
BONI	37.225	-117.1768	1.28	-3.38	0.09	0.11	MAGNET	9 Sep 2005
BROK	39.1688	-117.9426	1.09	-3.44	0.06	0.07	MAGNET	13 Apr 2006
BUFF	40.3614	-117.2662	-0.15	-3.25	0.08	0.06	MAGNET	19 Feb 2004
CALL	39.6878	-116.774	0.10	-2.73	0.08	0.08	MAGNET	19 Oct 2007
CEDA	40.6807	-112.8605	-0.90	-2.63	0.03	0.03	BARGEN	16 Jul 1996
CHNA	39.7203	-117.0619	0.28	-2.20	0.04	0.15	MAGNET	26 Oct 2006
CLAN	39.6651	-117.8972	0.41	-3.84	0.15	0.08	MAGNET	11 Aug 2004
CLOV	40.5584	-114.8742	-0.80	-2.89	0.09	0.09	PBO	17 Nov 2006
COLD	39.411	-117.8509	0.43	-3.33	0.04	0.06	MAGNET	26 Aug 2004
COON	40.6526	-112.121	-0.69	-1.81	0.05	0.05	BARGEN	16 Jul 1996
CRAM	37.0812	-116.8184	0.81	-2.92	0.06	0.04	BARGEN	15 Sep 2005
CRPL	38.7344	-117.5035	0.32	-3.18	0.09	0.09	MAGNET	8 Sep 2006
DRYC	38.6068	-117.33	0.99	-2.59	0.36	0.14	MAGNET	27 Sep 2006
DUNF	37.3136	-117.3089	1.46	-3.24	0.13	0.11	MAGNET	10 Sep 2005
ECHO	37.9155	-114.2642	-0.66	-2.71	0.04	0.04	BARGEN	29 May 1999
EGAN	39.3452	-114.9389	-0.79	-2.91	0.04	0.04	BARGEN	15 Mar 1997
ELKO	40.9147	-115.8172	-0.35	-3.38	0.03	0.03	BARGEN	23 Oct 1997
EPAS	37.9197	-117.8807	2.16	-3.20	0.25	0.26	MAGNET	9 Nov 2005
FOOT	39.3694	-113.8054	-0.68	-2.81	0.03	0.02	BARGEN	26 Mar 1997
GABB	38.9703	-117.9164	0.86	-3.35	0.04	0.03	BARGEN	23 Mar 1999
GEMF	37.745	-117.2985	0.49	-3.38	0.12	0.07	MAGNET	14 May 2005
GEOR	38.2223	-116.6877	0.02	-3.22	0.21	0.25	MAGNET	27 Sep 2006
GOLM	40.4618	-117.6005	0.58	-3.30	0.05	0.07	MAGNET	19 Feb 2004
GOSH	40.6402	-114.1797	-0.88	-2.86	0.03	0.07	BARGEN	21 Jul 1996
HANN	38.0978	-116.8981	0.47	-2.73	0.29	0.22	MAGNET	26 Sep 2006
HNTS	38.5031	-116.8387	-0.15	-2.49	0.25	0.20	MAGNET	27 Sep 2006
HOLT	38.4588	-117.9237	1.65	-2.86	0.12	0.09	MAGNET	13 Apr 2006
HURR	37.0639	-113.5747	0.21	-1.69	0.07	0.05	BARGEN	18 Sep 2005
HW50	39.4251	-116.7572	-0.25	-3.31	0.33	0.31	MAGNET	18 Oct 2007
HW95	37.1934	-116.9452	1.28	-3.07	0.12	0.14	MAGNET	9 Sep 2005
ICKY	38.8817	-117.7373	0.53	-3.43	0.04	0.09	MAGNET	8 Sep 2006
ICOR	37.4663	-117.2983	0.45	-3.52	0.08	0.13	MAGNET	13 May 2005
INKH	38.7359	-117.017	0.10	-3.06	0.65	0.09	MAGNET	27 Sep 2006
JERS	40.278	-117.4377	0.04	-2.87	0.08	0.10	MAGNET	19 Feb 2004
KITT	40.0626	-117.9123	0.92	-3.85	0.12	0.13	MAGNET	30 Sep 2004
KYLE	40.4014	-117.8548	0.86	-4.09	0.07	0.10	MAGNET	7 Oct 2004
LACR	40.8508	-115.7037	-0.29	-3.07	0.05	0.05	PBO	15 Nov 2006
LEWI	40.4035	-116.8619	-1.06	-1.85	0.07	0.06	BARGEN	27 Jul 1997
LTUT	41.5921	-112.2468	-1.36	-1.37	0.54	0.24	EBRY	2 Nov 2002
MANH	38.5031	-117.1807	0.39	-3.03	0.13	0.11	MAGNET	26 Sep 2006
MCKI	40.2085	-117.7838	0.72	-3.54	0.09	0.11	MAGNET	19 Feb 2004
MCOY	40.1179	-117.59	0.32	-3.39	0.09	0.06	MAGNET	19 Feb 2004
MILR	38.1199	-117.4419	0.92	-3.02	0.11	0.20	MAGNET	26 Sep 2006
MINE	40.1484	-116.0955	-0.42	-3.02	0.04	0.05	BARGEN	23 Oct 1997
MOIL	40.7107	-115.4121	-0.57	-3.03	0.10	0.06	PBO	16 Nov 2006
MONI	39.1477	-116.7156	-0.02	-2.96	0.06	0.05	BARGEN	16 Mar 1999
MONT	38.0778	-117.7084	1.52	-2.62	0.44	0.21	MAGNET	9 Nov 2005
MOUN	40.3034	-117.0695	-0.15	-2.21	0.10	0.06	MAGNET	19 Feb 2004
NAIU	41.0157	-112.2296	-0.92	-1.56	0.05	0.04	EBRY	15 Oct 1997
NEWS	39.6856	-117.5089	-0.05	-3.39	0.03	0.03	BARGEN	31 Oct 1997
NPAS	39.5821	-117.5358	0.30	-3.07	0.08	0.09	MAGNET	26 Aug 2004
OASI	37.0367	-116.7908	1.17	-2.96	0.08	0.06	MAGNET	9 Sep 2005
ORIE	37.2531	-117.4527	1.58	-3.61	0.10	0.10	MAGNET	10 Sep 2005

Table 1. (continued)

Station Name	Latitude	Longitude	Vn	Ve	Svn	Sve	Network	Day of First Data
P002	39.5211	-117.1865	0.08	-3.00	0.05	0.03	PBO	29 Sep 2006
P005	39.9102	-115.2786	-0.71	-2.86	0.07	0.07	PBO	23 Oct 2006
P007	41.7242	-114.8197	-0.80	-2.78	0.08	0.12	PBO	4 Nov 2007
P009	38.4799	-112.2227	-0.43	-1.48	0.16	0.25	PBO	31 Jan 2006
P013	41.4287	-117.33	0.29	-2.73	0.07	0.05	PBO	12 Apr 2007
P016	40.0781	-112.3614	-0.65	-2.61	0.07	0.05	PBO	15 Apr 2006
P057	41.7566	-112.6231	-1.02	-1.98	0.08	0.06	PBO	28 Aug 2004
P068	39.3056	-117.9848	0.89	-3.54	0.07	0.04	PBO	15 Nov 2006
P069	39.2879	-117.6049	0.36	-3.24	0.05	0.10	PBO	28 Sep 2006
P071	39.3465	-117.4012	0.11	-3.04	0.04	0.06	PBO	29 Sep 2006
P072	39.5215	-116.7409	-0.07	-2.96	0.09	0.09	PBO	21 Jun 2005
P073	39.5005	-116.4245	-0.12	-2.83	0.06	0.05	PBO	30 Sep 2006
P074	39.5464	-116.0496	-0.43	-2.82	0.14	0.06	PBO	1 Oct 2006
P075	39.3742	-115.8888	-0.44	-2.99	0.12	0.07	PBO	18 Oct 2006
P076	39.5361	-115.5126	-0.37	-2.83	0.05	0.06	PBO	19 Oct 2006
P077	39.3886	-115.4318	-0.64	-2.75	0.06	0.09	PBO	10 Apr 2008
P078	40.4334	-117.8798	0.96	-4.15	0.04	0.08	PBO	11 Apr 2007
P079	39.2552	-114.6917	-0.69	-2.60	0.20	0.13	PBO	5 Nov 2007
P080	39.1194	-114.2772	-0.66	-2.78	0.22	0.15	PBO	21 Oct 2006
P081	39.0673	-113.8713	-0.55	-2.87	0.06	0.04	PBO	14 Apr 2006
P082	39.2689	-113.5052	-0.73	-2.71	0.04	0.05	PBO	10 May 2006
P083	40.3206	-117.4676	0.12	-3.12	0.07	0.08	PBO	13 Apr 2007
P084	40.494	-113.054	-0.94	-2.69	0.05	0.06	PBO	18 May 2006
P085	40.4955	-116.7362	-0.49	-2.92	0.07	0.08	PBO	27 Sep 2006
P086	40.6488	-112.2821	-0.64	-2.31	0.07	0.07	PBO	15 Jan 2005
P087	40.3632	-116.2793	-0.14	-2.90	0.28	0.08	PBO	24 Oct 2006
P094	37.2008	-117.7042	2.54	-4.32	0.06	0.05	PBO	22 Nov 2006
P100	41.8568	-113.2942	-1.17	-2.76	0.25	0.17	PBO	29 Mar 2007
P102	39.9249	-115.556	-0.44	-2.95	0.28	0.09	PBO	20 Oct 2006
P103	39.3451	-113.0421	-0.71	-2.68	0.05	0.06	PBO	17 Jun 2008
P104	39.1861	-112.7171	-0.61	-2.37	0.08	0.06	PBO	13 Apr 2006
P105	39.3875	-112.5041	-0.15	-2.49	0.13	0.07	PBO	14 Sep 2004
P106	39.459	-112.2623	-0.49	-2.37	0.09	0.06	PBO	12 Apr 2006
P111	41.8173	-113.0122	-1.17	-2.70	0.06	0.06	PBO	14 Jun 2006
P113	40.6713	-113.278	-0.87	-2.71	0.05	0.05	PBO	17 Apr 2006
P114	40.634	-112.5276	-0.86	-2.47	0.07	0.08	PBO	31 Jul 2005
P115	40.4744	-112.428	-0.63	-2.60	0.18	0.12	PBO	27 Mar 2007
P116	40.434	-112.0142	-0.76	-2.14	0.08	0.10	PBO	3 May 2007
P121	41.8034	-112.6983	-1.37	-2.21	0.06	0.04	PBO	1 Jul 2004
P122	41.6354	-112.3319	-1.20	-1.61	0.05	0.05	PBO	28 Jun 2004
P469	37.2314	-117.9358	3.34	-5.11	0.08	0.06	PBO	19 Apr 2007
PACT	38.642	-117.803	1.02	-3.43	0.09	0.06	MAGNET	13 Apr 2006
PALO	40.0728	-117.1103	0.30	-2.81	0.08	0.07	MAGNET	24 Mar 2004
PHON	39.083	-117.7725	-0.24	-3.25	0.13	0.06	MAGNET	8 Sep 2006
PILO	38.2697	-117.9851	1.47	-3.21	0.17	0.12	MAGNET	16 Nov 2005
RAIL	38.2804	-115.6648	-0.32	-2.82	0.09	0.04	BARGEN	29 May 1999
REES	39.159	-117.3252	0.26	-3.10	0.07	0.10	MAGNET	8 Sep 2006
RHIL	38.4246	-117.5745	0.63	-3.09	0.13	0.06	MAGNET	8 Sep 2006
RICO	39.8841	-117.1057	0.45	-2.49	0.07	0.15	MAGNET	9 Sep 2006
ROJO	38.5767	-117.5463	0.43	-3.02	0.11	0.06	MAGNET	8 Sep 2006
ROYS	38.2626	-117.6066	1.06	-3.32	0.29	0.28	MAGNET	26 Sep 2006
RPAS	39.3586	-117.4128	0.22	-3.06	0.06	0.05	MAGNET	7 Sep 2006
RUBY	40.6172	-115.1228	-0.75	-2.90	0.03	0.03	BARGEN	21 Jul 1996
SANA	38.2445	-117.0816	1.06	-3.05	0.10	0.11	MAGNET	26 Sep 2006
SCOT	37.0606	-117.252	1.36	-3.52	0.08	0.07	MAGNET	10 Sep 2005
SHAK	37.2613	-117.9302	3.60	-5.04	0.63	0.61	MAGNET	1 Jul 2005
SHSH	39.8822	-117.729	0.13	-3.35	0.05	0.08	MAGNET	11 Mar 2004
SMEL	39.4256	-112.8449	-0.73	-2.51	0.03	0.03	BARGEN	26 Mar 1997
SPIC	39.3062	-112.1275	-0.30	-2.43	0.06	0.12	BARGEN	7 Feb 2003
SULF	37.2212	-117.6842	2.48	-4.34	0.23	0.22	MAGNET	1 Jul 2005
SYLV	37.4525	-117.7445	2.47	-4.18	0.12	0.08	MAGNET	13 May 2005

Table 1. (continued)

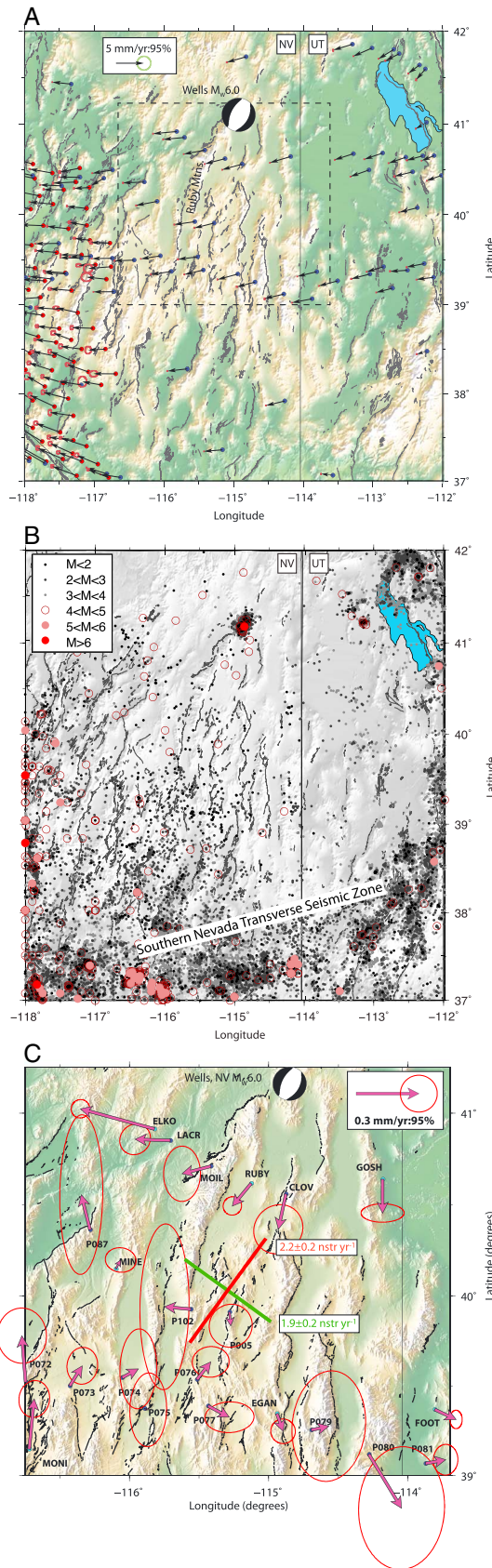
Station Name	Latitude	Longitude	Vn	Ve	Svn	Sve	Network	Day of First Data
THOM	37.9429	-117.375	0.91	-3.61	0.10	0.08	MAGNET	14 May 2005
TOIY	39.5422	-117.0494	-0.06	-3.08	0.04	0.06	BARGEN	7 Feb 2003
TONI	38.3582	-117.2926	1.50	-3.45	0.11	0.42	MAGNET	26 Sep 2006
TONO	38.0972	-117.184	0.49	-3.17	0.03	0.03	BARGEN	23 Mar 1999
TOYA	38.9107	-117.2356	0.71	-3.12	0.10	0.18	MAGNET	27 Sep 2006
UFOS	37.3988	-117.109	1.20	-3.72	0.06	0.07	MAGNET	14 May 2005
VIGU	39.5579	-117.1792	1.04	-3.04	0.21	0.07	MAGNET	24 Mar 2004
WEEP	37.85	-117.5689	1.66	-3.55	0.16	0.12	MAGNET	14 May 2005
WILC	40.5581	-117.8777	1.16	-4.14	0.08	0.10	MAGNET	7 Oct 2004
WOLF	37.6083	-117.8829	2.33	-4.62	0.11	0.13	MAGNET	13 May 2005
YOMB	38.9504	-117.517	0.22	-3.13	0.08	0.09	MAGNET	8 Sep 2006
ZUMA	37.5582	-117.4902	1.30	-3.50	0.10	0.10	MAGNET	13 May 2005

2.2. Analysis of Position Time Series

From the east and north time series, we calculated rates of motion with respect to North America by fitting the data with a model having intercept, slope, annual plus semiannual oscillations, and step function offsets for each known equipment change event. Damping is applied to each of the terms in the linear inversion for the time series model parameters, where the terms are set to be zero with an a priori uncertainty large enough to allow the expected range of values. Uncertainty of velocity was set to 10 mm yr^{-1} , in intercept to 10 m, in amplitude of annual and semiannual terms to 0.5 mm, in step sizes to 1 m. The importance of the damping parameters is large when the data sampling is insufficient to strongly constrain all parameters, as can be the case for seasonal terms in the MAGNET semicontinuous stations. The time of step events for each station is the set of unique times, where a receiver or antenna equipment was changed. For each of these cases, the time of the step was held fixed while the size of the step was estimated from the data. We edited the time series for obvious equipment-related effects. For example, an extreme change in time series behavior after an equipment change for station LTUT on 19 April 2008 prompted us to exclude all data before the change.

Uncertainties in rates were estimated with the CATS software, which employs a method that accounts for the effects of colored noise, seasonal terms, and equipment offsets in GPS time series [Williams, 2003]. We used a noise model that includes contributions from white and flicker noise, estimating the magnitude of contribution from each. The resulting rate uncertainties are sensitive to time series length (Figure 2). All uncertainties, for east and north rates, are less than 0.7 mm yr^{-1} ; stations with 10 years or more data have rate uncertainties less than 0.1 mm yr^{-1} . These rates are generally similar to those found by Davis *et al.*'s [2003] "whole error" method for BARGEN stations with time series up to 6 years duration. Although MAGNET stations tend to have higher uncertainties, this is mostly attributable to their shorter duration. Once MAGNET stations have duration of 5 or more years, they have similar levels of rate uncertainty compared to the continuous stations for a given time series duration (Figure 2).

The velocities with respect to North America have gradients that vary across eastern Nevada and western Utah (Figure 3). In western Utah, the velocity gradient across the Wasatch, Oquirrh, and Stansbury ranges is similar to that previously reported in several GPS studies [Martinez *et al.*, 1998; Hammond and Thatcher, 2004; Chang *et al.*, 2006], achieving a mean of 2.8 mm yr^{-1} west at the Nevada border and mean south rate for Utah stations west of -112° longitude of 0.8 mm yr^{-1} . Similar to previous studies [Niemi *et al.*, 2004; Kreemer *et al.*, 2010], we find that east-west velocity gradients associated with east-west extension persist west of the Stansbury range. The gradient in east-west velocity is $\sim 1 \text{ mm yr}^{-1}$ between -113° and -112° (west of the Wasatch). In Utah, the gradient in the east component is systematic and greater than the gradient in the north component, which is irregular. This suggests that the overall average signal of east-west uniaxial extension across these faults is modulated by complexity in crustal block motions (as noted in the detailed strain modeling study of Chang *et al.* [2006]). West of the NV/UT state line, the velocity gradients change character, with a near-zero increase in east component and an increase of $\sim 1 \text{ mm yr}^{-1}$ when moving west from -114° to -117° longitude. A component of this gradient west of -114° describes clockwise rotation and not deformation.



2.3. Mean Strain Rate Across the Central Basin and Range

Inspection of the velocities west of the Wasatch-Oquirrh-Stansbury domain of extensional deformation indicates that much of the signal is attributable to rotation. To isolate and visualize the velocity gradients that are attributable to deformation, we solve for the best fitting rigid rotation for all stations between -116.75° to -113.5° longitude and 39° to 41.25° latitude using the method of *Savage et al.* [2001]. The 24 stations in this region describe a best fitting Euler pole of rotation near $-124.6 \pm 2.4^\circ$ longitude, $63.6 \pm 3.2^\circ$ latitude, with a vertical axis spin rate of $0.064 \pm 0.009^\circ/10^6 \text{ yr}$. Removal of the signal of rigid rotation from the velocities reveals deformation rates that are greater than the uncertainties, that is well distributed across the BRP, and is dominated by shear (Figure 1c). There are no clear zones of concentrated deformation. Velocity gradients attributable to deformation are $\sim 0.6 \text{ mm yr}^{-1}$ over 300 km in the contraction and extensional directions. Principle strain rates are $1.9 \pm 0.2 \times 10^{-9} \text{ yr}^{-1}$ extension and $2.2 \pm 0.2 \times 10^{-9} \text{ yr}^{-1}$ contraction, with the direction of maximum extension oriented $N55^\circ W$. The sum of the principal components is zero to within uncertainty, indicating shear deformation. Although the strain rates are low, they are near an order of magnitude greater than the uncertainties and are supported by the signals in all 24 stations. Because of the combined rotation and shear, it is not sufficient to look at any single component of the velocity field to infer deformation and relate it to slip rates on active faults.

2.4. Strain Rates in Triangular Subnetworks

The previous analysis shows that GPS detects active tectonic shear strain in the central BRP, and hence, the velocities are inconsistent with microplate behavior. We can further constrain the

Figure 1. (a) Horizontal GPS velocity with respect to North America (NA12 reference frame) across the eastern Nevada, western Utah Basin and Range. The moment tensor beach ball marks the location and 21 February 2008 Wells, Nevada, M_w 6.0 earthquake epicenter. Red dots indicate MAGNET GPS stations; blue dots are continuous stations. Uncertainty ellipses at tip of vectors indicate 95% confidence in velocity. (b) Seismicity in our study area between 1932 and 2013 from the NCEC catalog (<http://www.ncedc.org/anss>). (c) Velocities with motion of best-estimated rigid block rotation removed. Magenta vectors show rotation-free deformation with northwest-southeast extension and northeast-southwest extension. Note the difference in velocity scale compared to Figure 1a. Faults are from *Haller et al.* [2004] Dashed box indicates extent of Figure 1c.

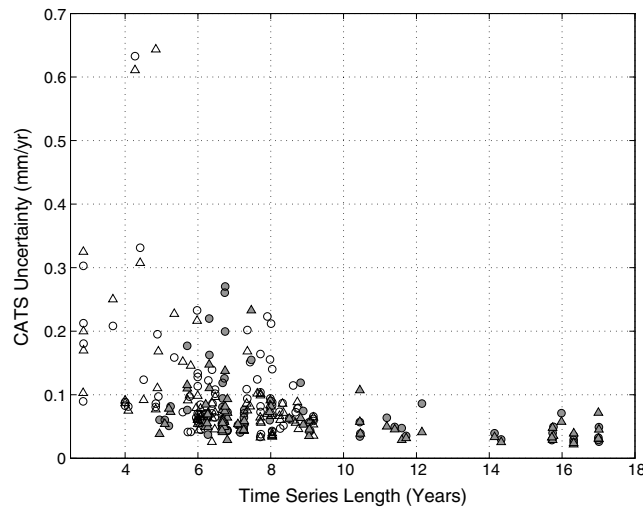


Figure 2. Velocity uncertainties for the east (triangles) and north (circles) components of horizontal velocity estimated using the CATS software. Shaded symbols are for continuous stations, open for MAGNET semicontinuous stations. The clusters of shaded symbols between 6 and 7 years duration represent PBO stations that were installed at the beginning of the EarthScope project.

distribution and variation of this deformation by considering the longest-running stations. Of those in Table 1, 47 stations have time series that are longer than 8 years and 22 have longer than 10 years (Figure 2). To estimate geographic variation in the strain rate and how the deformation varies with time over the interval of observation, we focus on the stations that have over 8 years of data and at least 50% complete time series. We additionally excluded two stations because of known influences of nontectonic affects. The station LEWI was likely affected by the pumping of water at the large open pit Cortez mine in Crescent Valley, Nevada [Gourmelen *et al.*, 2007], and the station P105 exhibits large vertical and horizontal displacements that are not seen at adjacent stations.

From the remaining 27 stations, we used their locations to generate a Delaunay triangulation of the network composed of 41 triangles (Figure 4). Of these triangles, some were poorly conditioned for strain analysis owing to small angles or side lengths resulting from short baseline distances between adjacent stations. We omitted triangles that had minimum angles less than 15° or shortest baseline less than 30 km. The remaining 27 triangles comprise 91% of the area tiled by the Delaunay triangulation and are used in the strain analysis.

For each triangle, we use the data from the days for which there was a position at all three stations. For each of these days, we calculate the displacement that occurred since the first common day. We use these six

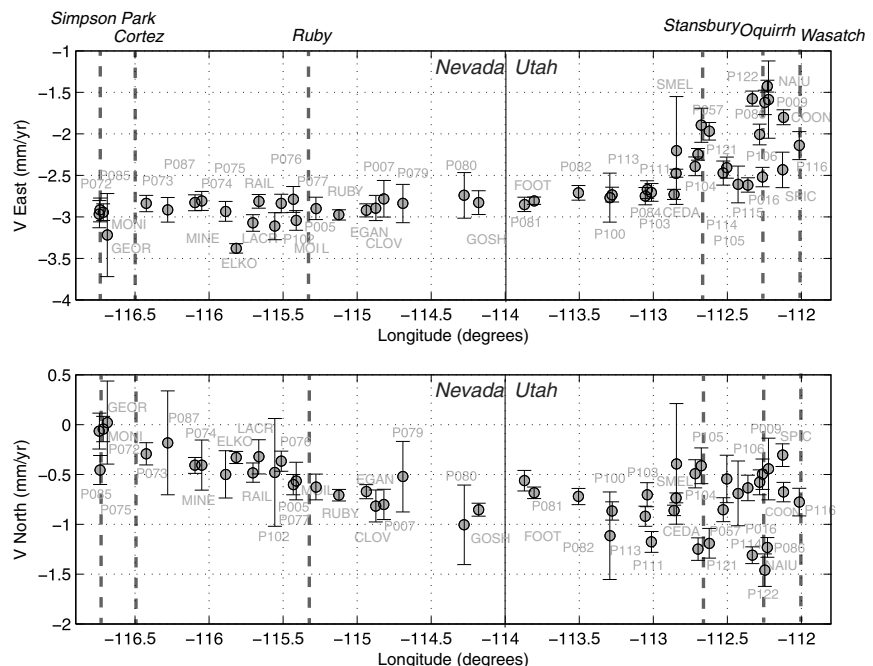
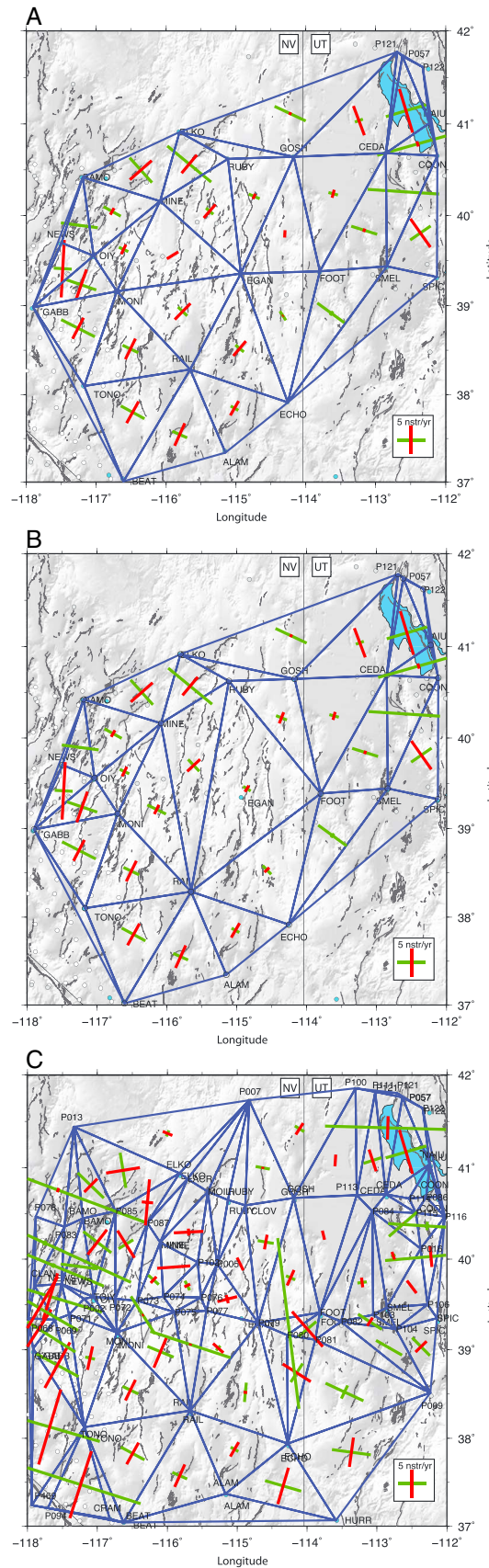


Figure 3. Velocity profile across eastern Nevada/western Utah Basin and Range. Uncertainty bars are 2σ . Light gray are station names. Dashed vertical lines are the names of selected mountain ranges.



cumulative displacements (three east and three north) to simultaneously estimate the components of rotation and tensor strain (not strain rate) that have occurred since the first common day using the method of *Savage et al.* [2001]. We estimate strain components for every common day resulting in time series of strain components. Advantages of this type of strain analysis include the following: (1) it does not make any prior assumption of a specific model (such as linear motion) for subnetwork shape change, as is needed for a regional filtering analysis [*Wdowski et al.*, 1997] and (2) shape change of station subnetworks is insensitive to common-mode noise that cause apparent shifts in the mean position of the network. The strain time series can be used to inspect the history and evolution of strain for each of the domains contained by the triangles. For each strain component, we solve for the slope, intercept, and seasonal terms, to estimate the strain rate. We include step discontinuities in the model for each day, where there was an antenna or receiver change or large earthquake nearby any of the three stations. The uncertainty in the strain rate is scaled by the RMS of the residual misfit of fit to the strain time series.

An example of the strain time series for the triangle defined by stations BEAT, RAIL, and TONO is shown in Figure 5. The estimated strain components are shown in Figures 5a–5c, while the shear ($e_1 - e_2$) and dilatation ($e_1 + e_2$) are shown in Figures 5d and 5e, where e_1 and e_2 are the derived maximum and minimum principle strains, respectively. The shear component of strain increases at $4.68 \pm 0.16 \times 10^{-9} \text{ yr}^{-1}$, while the dilatational component increases at $0.22 \pm 0.14 \times 10^{-9} \text{ yr}^{-1}$, consistent with this domain undergoing dilatation-free shear. The result shows a near linear progression of deformation from the beginning to the end of the time series. Step amplitudes were estimated in the motion model and removed before plotting, except for the step from the 21 February 2008 Wells, Nevada, earthquake which was left uncorrected to show its impact on the strain time series (Figure 5).

Figure 4. (a) Delaunay triangulation of long-running continuous GPS stations (over 8 years of duration) with horizontal strain rate tensors indicating contraction and extension direction and magnitude (red and green, respectively). Contraction and extension principal strain rates of equal magnitude represent shear deformation. (b) Same as Figure 4a but with a Delaunay triangulation that omits GPS station EGAN. (c) Same as Figure 4a but additionally includes stations with 4+ years of data duration.

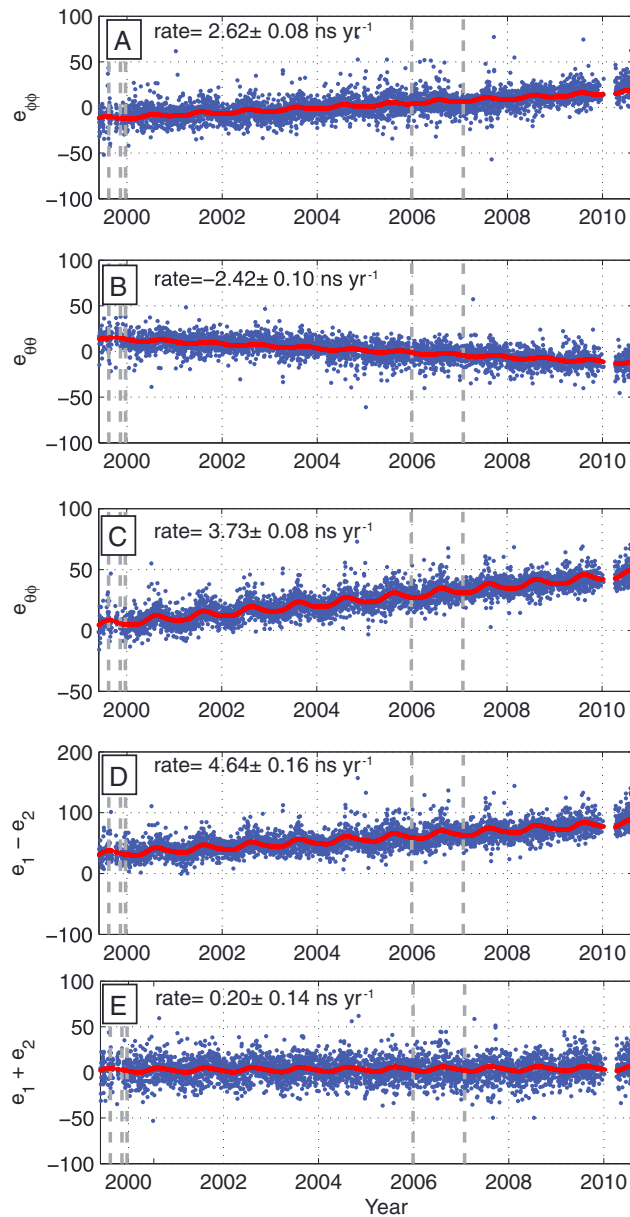


Figure 5. Example strain time series for subnetwork of GPS stations BEAT, RAIL, and TONO. (a) Longitude direction of strain $e_{\phi\phi}$, (b) latitude-longitude direction $e_{\theta\phi}$, (c) latitude $e_{\theta\theta}$ direction, (d) maximum shear strain $e_1 - e_2$, and (e) dilatational strain $e_1 + e_2$. Red line is best fitting model for time series that includes annual + semiannual terms and equipment-related steps.

defined by stations EGAN, MONI, and MINE, northwest of EGAN, has almost no extensional principal strain rate in contrast to almost every other subnetwork. To the southeast of EGAN, the strain rate is transitional between the uniaxial extension in Utah (in the FOOT, SMEL, and ECHO subnetworks) and shear in Nevada (the EGAN, RAIL, and ECHO subnetwork) but is missing the north-northeast contraction seen in the rest of Nevada. The strain time series of subnetworks that include EGAN shows motion that deviates from a straight line. This can be seen in systematic differences between the data and the best fitting linear plus seasonal terms plus equipment step model (Figure 6), making it clear that the source of this nonlinear motion is the common station EGAN. One of these subnetworks (FOOT-GOSH-EGAN) experienced significant coseismic deformation from the Wells, Nevada, earthquake.

Regional variations in tensor strain rates are estimated from the time series of strain components (Figure 4). In Utah, near the Wasatch-Oquirrh-Stansbury ranges, the strain rates vary in style and orientation, but the extension direction is consistently within 30° of east-west, broadly consistent with earlier detailed solutions for the Wasatch front and adjacent faults [Chang et al., 2006; Puskas et al., 2007; Kreemer et al., 2010]. In eastern Nevada, the principal strain rates are consistently less than $5 \times 10^{-9} \text{ yr}^{-1}$, having north-northeast contraction and west-northwest extension. The shear strain rates vary smoothly across adjacent triangular subnetworks, suggesting that the rates are stably and independently resolved. The level of uncertainty in strain rates is related to the uncertainties in the station's rates of motion. For example, the station RAIL, has a rate uncertainty of $<0.1 \text{ mm yr}^{-1}$. If RAIL moved 0.3 mm yr^{-1} more rapidly westward, it would completely remove the east-west extensional strain rate component in the RAIL-MONI-MINE triangular subnetwork and differ from the regional pattern. Thus, the smoothly varying pattern of tensor strain rate, orientation, and styles suggests that the velocity uncertainties of 0.1 mm yr^{-1} (Table 1) are plausible. These are consistent with the uncertainties estimated from the strain time series, often $<0.1 \times 10^{-9} \text{ yr}^{-1}$ (Table 2), which is equivalent to 0.1 mm yr^{-1} rate over 1000 km.

Around the GPS station EGAN, the strain rates deviate from the average orientation of shear strain in eastern Nevada. The subnetwork triangle

Table 2. Tensor Strain Rates Inside Three-Station Subnetworks (10^{-9} yr^{-1})

Station Trios	$e_{\varphi\varphi}$	$e_{\theta\theta}$	$e_{\theta\theta}$	e_1	e_2	e_{Δ}	e_{shear}
NAIU-P057-CEDA	14.44 ± 0.71	-3.79 ± 0.34	-4.91 ± 0.27	14.64 ± 0.67	-5.37 ± 0.30	9.76 ± 0.76	19.71 ± 0.71
FOOT-ECHO-SMEL	4.33 ± 0.22	1.69 ± 0.15	0.62 ± 0.17	1.89 ± 0.14	2.98 ± 0.23	4.94 ± 0.28	-1.10 ± 0.27
GOSH-FOOT-CEDA	1.35 ± 0.16	1.37 ± 0.08	-1.29 ± 0.08	1.58 ± 0.17	-1.51 ± 0.07	0.06 ± 0.19	3.07 ± 0.19
P114-SMEL-SPIC	1.10 ± 0.28	-2.82 ± 0.11	-2.29 ± 0.08	0.11 ± 0.26	-1.32 ± 0.10	-1.17 ± 0.30	1.32 ± 0.21
RAIL-FOOT-RUBY	0.94 ± 0.09	1.35 ± 0.06	-0.44 ± 0.07	1.32 ± 0.09	-0.82 ± 0.06	0.51 ± 0.11	2.13 ± 0.10
RAIL-MONI-TONO	1.75 ± 0.10	2.89 ± 0.08	-2.66 ± 0.10	2.97 ± 0.12	-3.90 ± 0.09	-0.92 ± 0.13	6.86 ± 0.17
TONO-MONI-GABB	4.43 ± 0.11	4.48 ± 0.07	-1.88 ± 0.09	5.06 ± 0.11	-2.51 ± 0.10	2.55 ± 0.14	7.58 ± 0.15
TONO-BEAT-RAIL	2.65 ± 0.12	3.73 ± 0.08	-2.42 ± 0.10	2.47 ± 0.11	-2.23 ± 0.10	0.22 ± 0.14	4.68 ± 0.16
MINE-RUBY-ELKO	3.34 ± 0.24	6.77 ± 0.15	1.81 ± 0.18	8.31 ± 0.27	-3.15 ± 0.15	5.16 ± 0.32	11.46 ± 0.30
MONI-RAIL-MINE	2.82 ± 0.48	2.25 ± 0.23	-0.99 ± 0.23	2.09 ± 0.33	-0.33 ± 0.35	1.88 ± 0.54	2.37 ± 0.43
GABB-MONI-TOIY	4.48 ± 0.32	3.50 ± 0.35	-4.84 ± 0.40	1.80 ± 0.43	-1.95 ± 0.34	-0.29 ± 0.58	3.84 ± 0.50
NEWS-TOIY-BAMO	7.34 ± 0.33	0.26 ± 0.16	0.11 ± 0.11	6.94 ± 0.31	0.49 ± 0.13	7.44 ± 0.34	6.16 ± 0.30
P072-MINE-BAMO	2.07 ± 0.15	2.15 ± 0.10	-0.66 ± 0.19	1.03 ± 0.17	0.39 ± 0.15	1.41 ± 0.22	0.65 ± 0.23
GABB-TOIY-NEWS	2.73 ± 0.60	0.49 ± 0.35	-10.49 ± 0.49	1.98 ± 0.64	-9.73 ± 0.39	-7.75 ± 0.81	11.71 ± 0.69
BAMO-MINE-ELKO	-0.23 ± 0.14	5.32 ± 0.12	1.25 ± 0.21	1.82 ± 0.21	-0.81 ± 0.14	1.02 ± 0.26	2.60 ± 0.24
ELKO-GOSH-P121	4.26 ± 0.13	1.83 ± 0.16	-1.08 ± 0.18	4.52 ± 0.12	-1.33 ± 0.23	3.18 ± 0.25	5.75 ± 0.22
P121-GOSH-CEDA	-1.61 ± 0.39	-3.11 ± 0.20	-5.57 ± 0.23	-0.87 ± 0.33	-6.26 ± 0.29	-7.15 ± 0.46	5.44 ± 0.40
RUBY-MINE-RAIL	-1.36 ± 0.45	3.76 ± 0.24	0.56 ± 0.18	3.10 ± 0.37	-4.02 ± 0.30	-0.84 ± 0.49	6.94 ± 0.47
CEDA-FOOT-SMEL	3.64 ± 0.20	1.77 ± 0.14	-0.88 ± 0.13	3.18 ± 0.19	-0.50 ± 0.12	2.80 ± 0.23	3.66 ± 0.22
GOSH-RUBY-FOOT	1.39 ± 0.24	0.99 ± 0.10	-1.10 ± 0.10	-0.71 ± 0.10	0.99 ± 0.22	0.30 ± 0.24	-1.68 ± 0.26
ALAM-RAIL-BEAT	1.61 ± 0.12	2.76 ± 0.09	-3.08 ± 0.15	0.49 ± 0.13	-1.92 ± 0.12	-1.47 ± 0.20	2.42 ± 0.16
ECHO-FOOT-RAIL	0.39 ± 0.12	1.62 ± 0.09	0.46 ± 0.11	1.13 ± 0.12	-0.28 ± 0.11	0.85 ± 0.17	1.41 ± 0.14
ECHO-RAIL-ALAM	0.34 ± 0.11	1.99 ± 0.11	-1.94 ± 0.16	0.93 ± 0.12	-2.53 ± 0.14	-1.57 ± 0.21	3.45 ± 0.16

Removing EGAN from the Delaunay triangulation and repeating the analysis show that all strain rates in triangles in eastern Nevada have similar tensor style and orientation (Figure 4b). Taken together, the differences from the regional shear deformation and the visual inspection of the time series for EGAN suggest that EGAN experiences motions that are not shared by adjacent stations. Although the average rate of EGAN is similar to that of adjacent stations (Figure 3), its nonlinear wander is greater than adjacent stations and is manifested in the very sensitive measurements of deformation available in the triangle subnetwork analysis. This wander is north and west, reducing the northwest extension in domains to the northwest (e.g., EGAN-MONI-MINE) and the north-northeast contraction in EGAN-ECHO-FOOT. The strain rates provided (Table 2) are for the triangulation that excludes EGAN.

Further improving the geographic resolution of the strain rate analysis could shed light on whether EGAN is anomalous (as in local or equipment-related effects) or experiences effects of a transient deformation contained within the zone of nearest long-running continuous stations. To improve the resolution, we could use more stations, i.e., the PBO stations, which have a relatively high density across eastern Nevada, near latitude 39°. However, introducing these stations reduces the stability of the strain estimates because (1) the triangles frequently include stations that have shorter time series (<8 years) and (2) the triangles become smaller, so baseline distances are shorter, which reduces the signal-to-noise ratio of shape change in each triangle. This can be seen in increased scatter of strain rate estimates in the network that includes all stations (Figure 4c), where strain estimate of smaller triangular subnetworks tends to differ more from the regional pattern.

2.5. Testing the Active Megadetachment Hypothesis

It has been suggested that large subcontinental scale transient deformations have occurred during the period of GPS observation in the BRP [Davis *et al.*, 2006; Wernicke *et al.*, 2008]. The idea is that large sections of the BRP crust have episodically translated horizontally, increasing then decreasing the velocity of clusters of GPS stations that span many fault systems. The active megadetachment class of deformation would predict nonlinear movements of GPS station positions that are aligned to a stable external reference frame (e.g., NA12). However, measurements of relative station position, as discussed in the strain analysis above, discard signals of network translation and focus on deformation. Transient deformation will be observed near the boundaries of an episodically translating rigid or quasi-rigid domain.

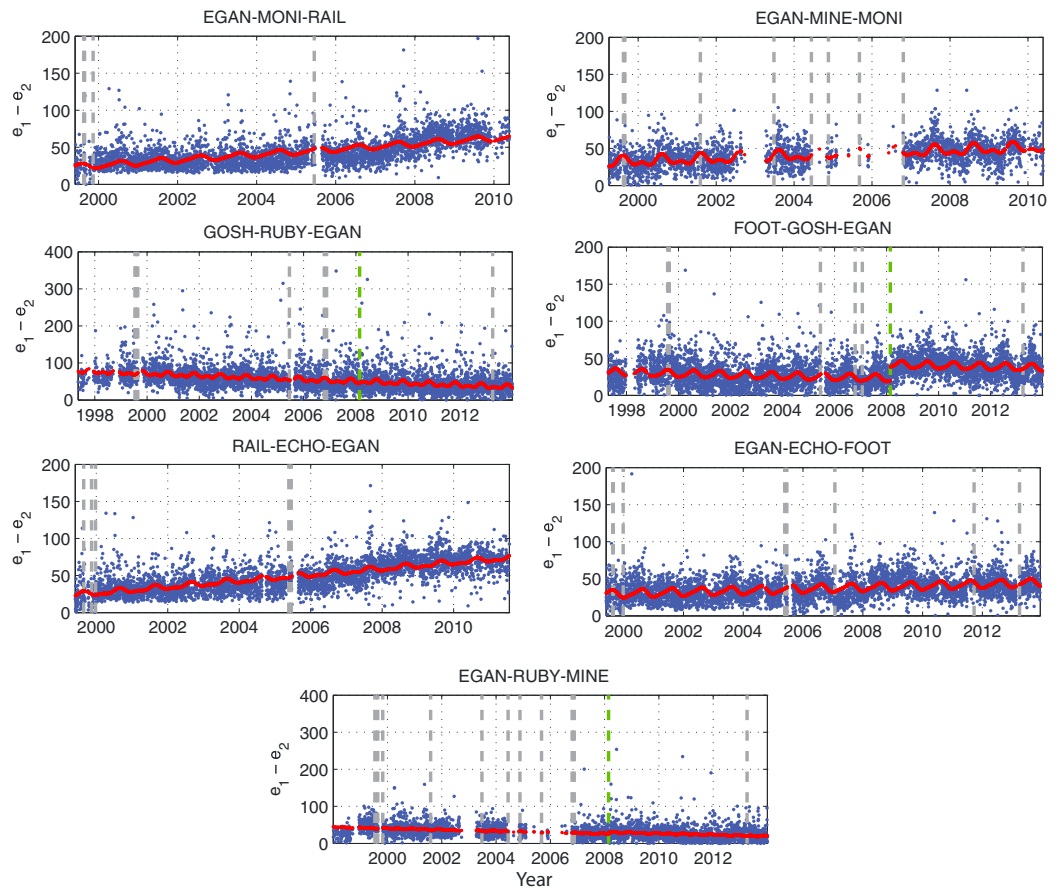


Figure 6. Time series of shear strain component ($e_1 - e_2$) for each of the triangles that includes station EGAN. Annotation in each panel indicates the three stations used to estimate the cumulative strain since the first day. Nonlinear motions of EGAN are especially evident after equipment changes that occurred in year 2005. Gray dashed lines show time of equipment change in at least one of the three stations. Green dashed line indicates time of Wells, Nevada, M_W 6.0 earthquake.

We focus on two predictions of the active megadetachment hypothesis: (1) the existence of quasi-rigid domains that translate episodically and (2) the signal of episodic deformation near the boundaries of a rigid domain. To address the first point, we focus our analysis on deformation. The movement of a quasi-rigid domain predicts that time series of strain for any set of stations that lie on it, whether it moves constantly, episodically, or not at all, will result in strain time series whose slope is zero, i.e., strain rate estimates that are not significant. However, we observe the opposite. We observe well-distributed nonzero strain rates across eastern Nevada and western Utah that are significantly different that zero (Figure 4). There is no set of three adjacent stations for which we can confidently conclude rigid behavior. The possible exceptions are the EGAN-ECHO-FOOT and EGAN-FOOT-GOSH subnetworks, where strain rates are smallest but are likely affected by motion attributable solely to EGAN. If unsteady motion of EGAN is attributable to episodic motion on an active detachment, then the geographic extent of the detachment is limited to be inside the set of stations in Figure 4a surrounding EGAN. This is much smaller than the domain described by *Wernicke et al.* [2008], which extended from the Utah border, spanning Nevada to the Sierra Nevada.

To address the second point, we search for the signal of geographically focused episodic deformation near the boundaries of a rigid domain. The active megadetachment hypothesis predicts strain signals that will deviate from secular background deformation. The absence of nonlinear effects in the time series would suggest that the deformation is characterized by steady secular deformation rather than episodic deformation. The latter is closer to what we observe. Because quantitative estimation of misfit of time series to linear plus seasonal terms plus steps models does not clearly distinguish between systematic nonlinear excursions of the time series from (e.g., in EGAN), we rely on visual inspection of time series of residual strain

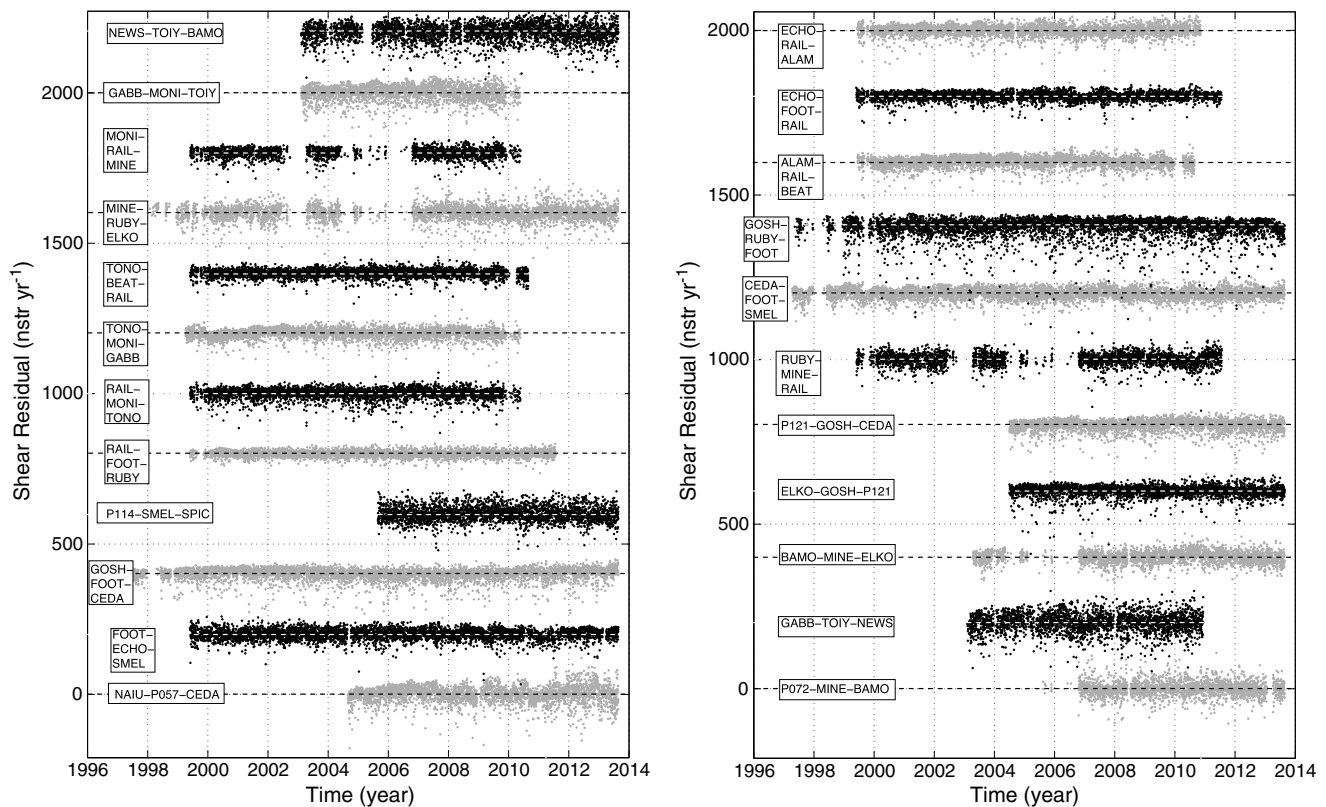


Figure 7. Residuals for all (a) shear strain ($e_1 - e_2$) time series after the model of linear plus seasonal plus equipment steps terms has been removed. (b) Same as Figure 7a but for dilatation component of strain ($e_1 + e_2$). Delaunay triangulation is for the set of stations that excludes EGAN. Annotation in each figure shows which three GPS stations were used. Vertical offset of time series is arbitrary in order to show time series on same plot axes. Dot color is alternated between black and gray to distinguish adjacent time series.

rates to ascertain if systematic excursions, wanders, indicate nonlinear behavior. The residual time series are shown in Figure 7. While some examples of deviations from steady linear behavior exist, they are in almost all cases plausibly explained by discontinuities in GPS equipment, such as receiver, antenna, or radome changes. The signal of any transient deformation would appear in these time series as systematic wanders in the residual time series, but our visual inspection does not confidently reveal any. In summary, the pattern of strain time series does not support the active megadetachment hypothesis. In contrast, the data do support a model of steady, continuous deformation everywhere in the BRP.

2.6. Viscoelastic Relaxation From the Twentieth Century Earthquakes in Nevada

Over the last century, a belt-like cluster of large earthquakes occurred in central Nevada, together releasing most of the seismic moment recorded in the Basin and Range over historic time [Wallace, 1984; Doser, 1988; Bell et al., 2004]. The source region, known as the Central Nevada Seismic Belt (CNSB), is the locus of a transient postseismic deformation that has been detected geodetically with GPS and interferometric synthetic aperture radar [Gourmelen and Amelung, 2005; Hammond et al., 2012] and modeled as a viscoelastic response to the coseismic stress change in the crust and upper mantle [Hetland and Hager, 2003]. Postseismic deformation can have far-reaching impacts with perturbations in deformation rates that can extend hundreds of kilometers or farther from the epicenters [e.g., Freed et al., 2007; Pollitz et al., 2008; Hammond et al., 2010]. Since these effects are measurable in central Nevada, we consider the possibility that far-field viscoelastic relaxation following these earthquakes is contributing to the strain we detect in eastern Nevada. Some of the CNSB earthquakes had components of dextral slip, which could provide a postseismic dextral shear similar to what we observe with GPS if it extends far enough and persists for long enough to be detected.

To estimate the expected strain rate from viscoelastic relaxation in each of the triangular subnetworks, we use the VISCO1D software of Pollitz [1997]. We incorporate a simple elastic and viscoelastic structure where

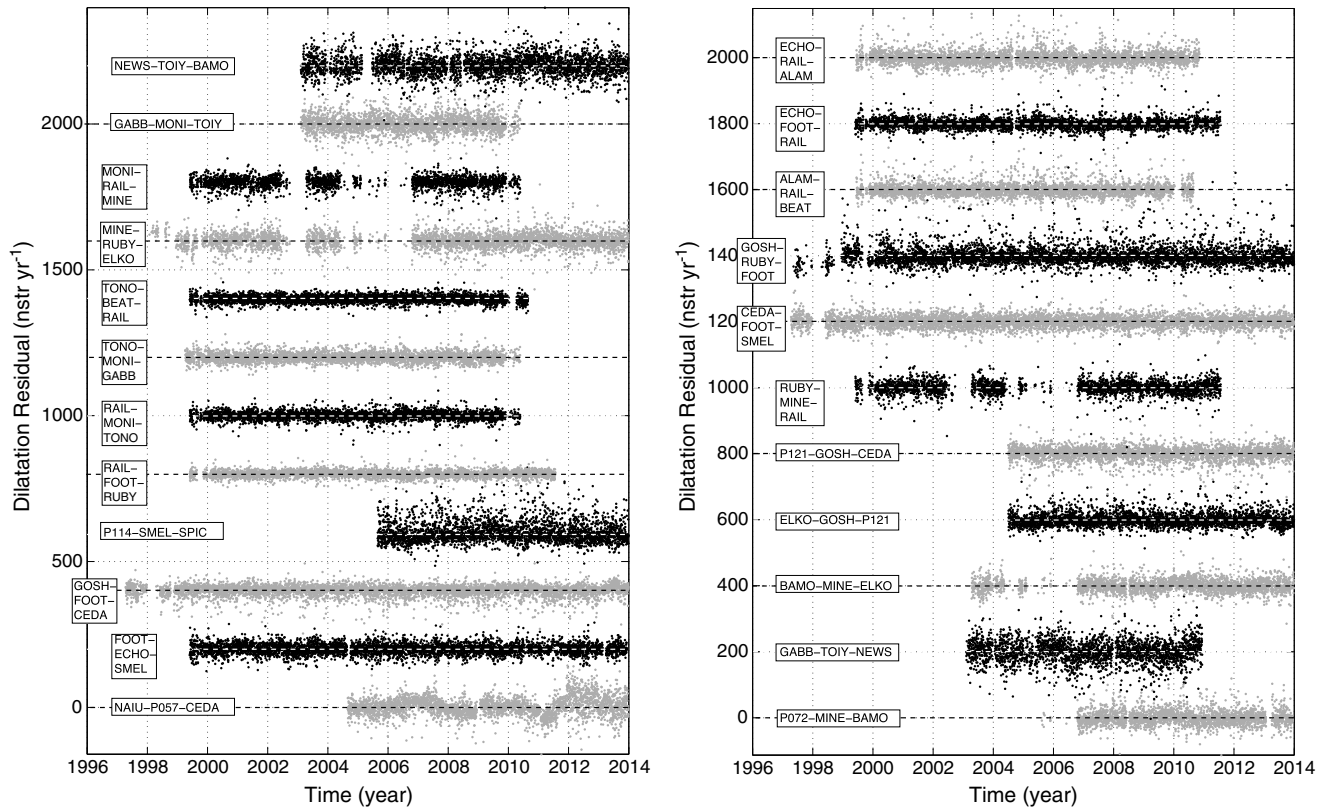


Figure 7. (continued)

the Earth is divided into three layers, a topmost elastic (0–15 km depth), a Maxwell viscoelastic lower crust (15–30 km), and a third layer representing the uppermost mantle (>30 km). Following *Hammond et al.* [2009], we iterate through viscosities between 10^{17} and 10^{21} Pa s in logarithmic steps of 1/2 order of magnitude assuming the same source mechanisms for the CNSB earthquakes. We calculate model position time series for each location on a grid of $0.25^\circ \times 0.25^\circ$ throughout Nevada and Utah and interpolate the displacements to the location of the GPS stations. Using the same methodology we applied to the GPS time series, we estimate rates of motion and strain rates inside each of the triangular subnetworks in Figure 4.

To evaluate whether any of the models of postseismic viscoelastic relaxation plausibly explain the strain rate observed in eastern Nevada and western Utah, we calculate a measure of misfit between model and data using

$$\chi^2 = \sum_{i=1}^N \left[(e_{\varphi\varphi,i,obs} - e_{\varphi\varphi,i,ps})^2 + (e_{\theta\theta,i,obs} - e_{\theta\theta,i,ps})^2 + (e_{\theta\varphi,i,obs} - e_{\theta\varphi,i,ps})^2 \right] \quad (1)$$

where $e_{\varphi\varphi}$, $e_{\theta\theta}$, and $e_{\theta\varphi}$ denote the strain rate components in the colatitude (θ) and longitude (φ) directions [*Savage et al.*, 2001], and the subscripts *obs* and *ps* denote the observed and model postseismic strain rates, respectively. The summation is applied over the N subnetworks of the Delaunay triangulation. The misfit is a function of the assumed viscosities (Figure 8). The minimum value for χ is $21 \times 10^{-9} \text{ yr}^{-1}$, much larger than the uncertainties in the data indicating a poor fit between the best model and the data. The best fitting model has strain rates that are far smaller than the observed strain rates in eastern Nevada.

That best fitting model has a strong upper mantle (viscosity of 10^{21} Pa s) and a weak lower crust (viscosity of 10^{18} Pa s). These values differ from what has been found in earlier studies of postseismic viscoelastic transient deformation, where viscosities are typically lower in the mantle than in the crust (see, e.g., summary by *Thatcher and Pollitz* [2008]). This, and the fact that the best model does not fit well, suggest that the observed strain rates are not due solely to viscoelastic relaxation from the CNSB earthquakes. However, we acknowledge that the set of models for postseismic deformation that we have tested is small compared to the number of possibilities. For example, more complicated Earth models including nonlinear power law

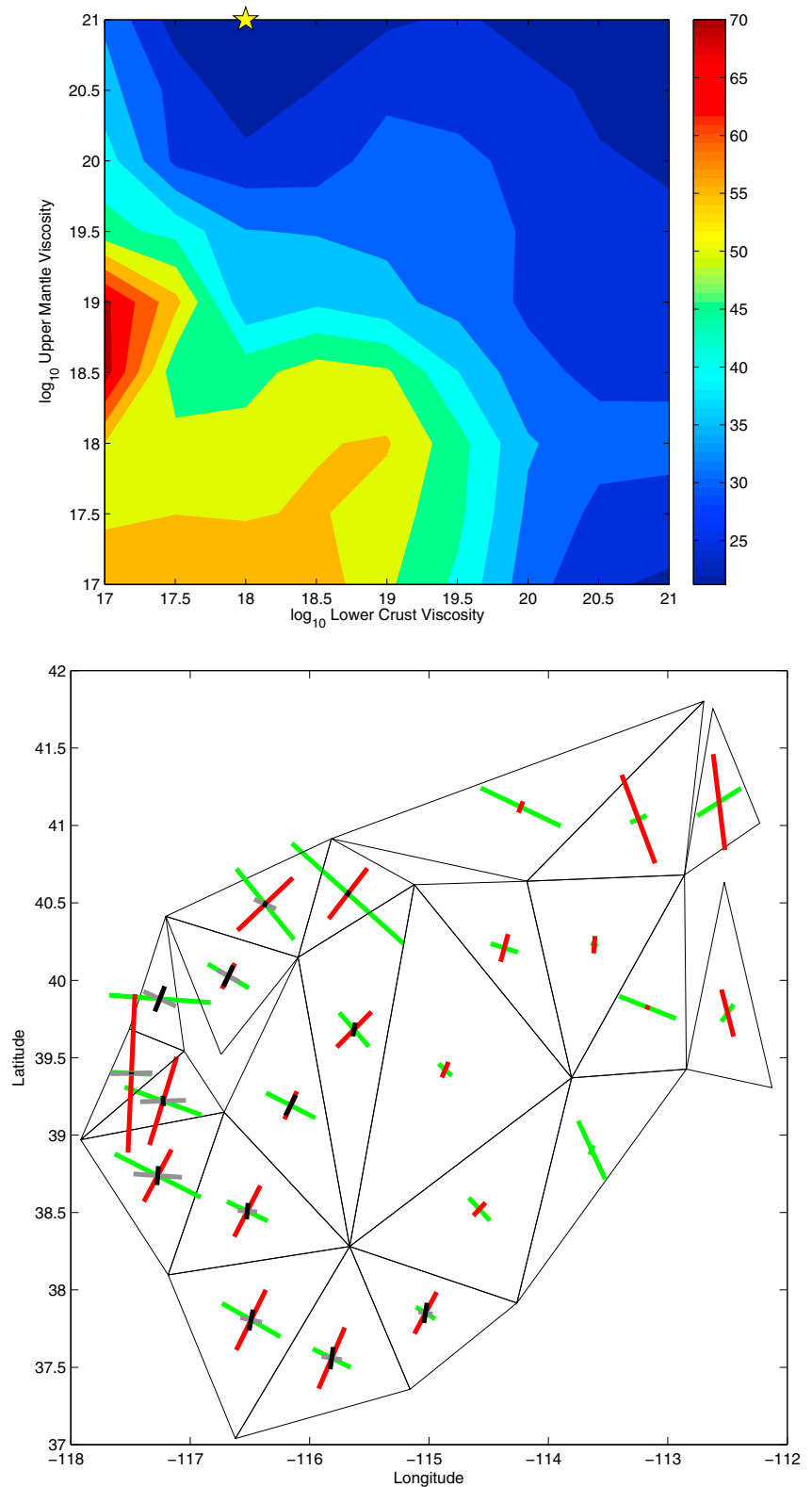


Figure 8. (a) Contour plot showing misfit for each of the viscoelastic postseismic relaxation models tested. Color shows misfit between GPS data and model with indicated lower crust and upper mantle viscosity. Yellow star shows best fitting model at $\eta_{UM} = 10^{21}$ Pa s, $\eta_{LC} = 10^{18}$ Pa s. (b) Comparison between measured strain rates from Figure 4b (red = contraction, green = extension) and best fitting strain rates from viscoelastic postseismic relaxation model (black = contraction, gray = extension).

rheology, transient rheology, or lateral variations in elastic and viscous properties of the earth could provide different patterns that could better match the observations.

3. Discussion

3.1. Strain Rates Low but not Zero

GPS observations show that crustal deformation is not restricted to the perimeter of the BRP, but appears to be distributed throughout its interior, though at lower rates. All regions deform at rates significantly greater than zero (Table 2). Furthermore, these deformation rates appear to be reasonably constant over the period of GPS observation, which is a characteristic of tectonic deformation. The Great Basin deforms everywhere and all the time.

This finding is consistent with the occurrence of diffuse seismicity that is present in earthquake catalogs. Within our study area, we found over 34,000 earthquakes (Figure 1b) in the catalog of the Advanced National Seismic System that occurred between 1932 and 2013 [<http://www.ncedc.org>, accessed September 2013]. Many of the events are concentrated along the southern Nevada transverse seismic zone that crosses southern Nevada near the southern end of our study area [Slemmons *et al.*, 1965]. It has been proposed that this seismicity is a part of a throughgoing kinematic connection between east-west extensional deformation associated with the Wasatch fault zone and the rest of the Pacific/North America plate boundary in the eastern California shear zone [Kreemer *et al.*, 2010]. This zone is thought to accommodate up to 1.8 mm yr^{-1} across the Pahrnagat shear zone (PSZ). Our results indicate that this deformation also extends north of the PSZ. The strain rate map in Figure 1 of Kreemer *et al.* [2010] allows for lower intensity, single-digit $\times 10^{-9} \text{ yr}^{-1}$ deformation, similar to Figure 4. However, we image a smoother geographic variation, possibly because we use only the geographically less dense longest-running continuous GPS stations. The deformation we image is not attributable solely to the PSZ since we find strain west, and northwest of station RAIL, well north of the PSZ.

Other recent results from western U.S.-scale models designed to evaluate seismic hazard favor an actively deforming Basin and Range. While none of these have focused exclusively on the eastern Nevada/western Utah, as we do in this study, strain rates determined by different research groups using different analysis methods (blocks, deformable blocks, and continuum) found strain rates between 1 and $10 \times 10^{-9} \text{ yr}^{-1}$ [Petersen *et al.*, 2014]. Payne *et al.* [2012] conducted an analysis of GPS data throughout the northwest United States surrounding the Snake River Plain, with significant overlap with our area in northern Nevada and Utah. Based on a combination of campaign and continuous GPS data, they found rates of deformation similar to ours, $3.5 \pm 0.2 \times 10^{-9} \text{ yr}^{-1}$ on average for a broad domain that spans all of northeast Nevada and western Utah north of latitude 40° . They found the west-northwest extension greater than the north-northeast contraction, possibly because their large block includes several distinct deformation domains, including the northern Wasatch and central Nevada Seismic Belt. We see a significant change of strain rate and style from east to west across this area, showing the need to allow for geographic variation of strain rates.

Our study places new lower bounds on rates of deformation that can be detected and characterized using GPS-based crustal deformation observatories. While a few studies have reported uncertainties in strain rates less than $1 \times 10^{-9} \text{ yr}^{-1}$ [e.g., Calais *et al.*, 2006; Berglund *et al.*, 2012; Payne *et al.*, 2012], these are typically mean deformations across wide domains of hundreds of kilometers using many stations. We report uncertainties significantly below $1 \times 10^{-9} \text{ yr}^{-1}$ for three-station subnetworks with long (up to 18 years) of observation. The regional consistency of the strain rate estimates across the BRP suggests that the signals of crustal deformation are greater than the uncertainties in the estimates. These analysis techniques may be useful for detecting very low strain rates in other locations, such as the U.S. midcontinent, where earthquakes with magnitude near 8 have occurred though the background tectonic strain has remained difficult to detect [e.g., Newman *et al.*, 1999; Stein, 2007].

3.2. Implications for Slip Rates and Seismic Hazard

The implications this study has for seismic hazard are twofold. First, strain accumulation is active throughout the BRP. The budget for Pacific/North America plate boundary deformation east of the Sierra Nevada must include the strain across the central BRP. Several lines of evidence support the argument that this deformation will eventually be released in future earthquakes. The azimuths of strain rate axes closely resemble the maximum and minimum compressive stresses inferred from seismic moment tensors [Patton and Zandt, 1991] and

interpolations of the World Stress Map [Heidbach *et al.*, 2009]. In particular, the Wells, Nevada, M_W 6.0 (Figure 1) earthquake had a T axis direction of extension subparallel to the direction of principal extension suggesting consistency between strain accumulation and seismic strain release [Smith *et al.*, 2011]. In the diffuse microseismicity that is distributed across the central BRP (Figure 1b), there is some correlation between the density of earthquakes and the strain rates, with generally fewer events where strain rates between -115° and -113° longitude are lower and west of -115° longitude where shear strain rates increase, suggesting that the measured deformation is related to seismicity. Finally, a paleoseismic transect that crossed the BRP at latitude 39° north summed east-west extension rates from trenches across 11 range-bounding faults near the southern edge of our study area [Koehler and Wesnousky, 2011]. They found a cumulative extension rate of between 0.8 and 1.0 mm yr^{-1} , similar to the variation in GPS velocity we show in Figure 3. The geographic distribution of the longest running GPS stations is sparse ($\sim 100 \text{ km}$ in Figure 4b) compared to the spacing of geologically active faults, and thus, we cannot resolve individual slip rates. However, the geologic data suggest that deformation will be accommodated primarily on faults approximately evenly distributed within the triangular domains, consistent with long-term deformation found not “everywhere” but focused on active faults.

We have considered the possibility that strain accumulation from more rapidly slipping faults in the far field (e.g., San Andreas) can give the impression of strain accumulation on BRP faults. We can estimate these effects using a simple calculation based on the arctangent-buried dislocation model of a strike-slip fault [Savage and Burford, 1973]. Assuming a fault locked to a depth of 15 km, the slipping 35 mm yr^{-1} provides less than 0.1 mm yr^{-1} of over 300 km in eastern Nevada, smaller than what is observed, and thus cannot account for the observed strain rates.

Second, shear deformation, that is the predominant signal in the GPS data, suggests that the geologic evidence of past vertical offset from normal faulting may not record all of the seismic moment released. In paleoseismology, horizontal strike-slip offsets can be more difficult to observe than vertical separation, so estimates of slip style may be biased toward pure normal. The situation may be analogous to the Walker Lane to the west, which undergoes more rapid transtension. Along the normal fault-bounded basins from Tahoe to the Wassuk Range, the normal component of geologic separation is consistent with the local rate of geodetic extension, but there is only rare strike slip to match the measured geodetic shear [Kent *et al.*, 2005; Wesnousky *et al.*, 2012; Bell *et al.*, 2012; Bormann *et al.*, 2012]. The detailed modeling of this system suggests that some dextral slip is required and that block rotations alone are not sufficient to accommodate the shear [Bormann, 2013]. Some earthquakes in the CNSB, a region transitional between the Walker Lane and BRP, had a component of dextral oblique normal slip. For example, the 1954 Fairview Peak M_W 7.0 event had dextral oblique slip on an east dipping normal fault, and the Cedar Mountain M_W 7.1 1932 event was predominantly dextral [Doser, 1988]. The shear strain that we detect with GPS suggests that oblique slip style may be a common mode of rupture across the BRP and contribute significantly to the budget of seismic moment release.

3.3. Continental Dynamics

Traditionally, motion and deformation of the BRP have been ascribed to a combination of shear tractions through the plate boundary and gravitational forces associated with density and crustal thickness contrasts within the lithosphere [e.g., Jones *et al.*, 1996; Flesch *et al.*, 2000; Zoback and Mooney, 2003; Thatcher, 2009], while basal tractions may play a smaller but guiding role [e.g., Silver and Holt, 2002; Humphreys and Coblenz, 2007; Gosh *et al.*, 2013]. The style and azimuth of deformation we observe suggest an affinity with Pacific North America plate boundary traction. England *et al.* [1985] showed that for a thin viscous lithosphere, the distance to which plate boundary edge-driven shear deformation penetrates into the continent is expected to be shorter than that for deformation applied normal to the boundary. However, we find that shear deformation penetrates at least 800 km into the North American continent, almost but not quite as far as the measureable extension. While dynamic studies show that gravity plays an important role in the westward collapse of western U.S. lithosphere toward the Pacific, our results suggest that plate boundary tractions are the dominant source of driving stress as far east as eastern Nevada. The signal of gravitational collapse may be present but overprinted by the western plate boundary. This supports the conclusions of Parsons and Thatcher [2011], who found that extension and shear rates can be reconciled using models that include reasonable strength profiles, simple boundary conditions for the North American lithosphere and a rigid Sierra Nevada/Great Valley microplate that help lengthen the inboard reach of shear stress from the Pacific.

However, east of the Nevada/Utah border, the deformation style changes to be more consistent with the east-west uniaxial strain rate. Thus, if the strain style is sensitive to the source of driving forces, e.g., shear from the plate boundary and extension from gravity, we would infer that the point of tradeoff between the relative importance of these factors is near the Nevada/Utah border. With the balance toward shear west of longitude -112° and toward extension eastward, e.g., at the Wasatch and Rio Grande Rift.

4. Conclusions

Our study shows that new data from a greater number of GPS stations provide a new lower detection threshold for crustal strain rates in the Basin and Range. The data reveal active deformation across the central part of the province, inconsistent with microplate behavior. Velocity change attributable to deformation is about 0.6 mm yr^{-1} over 300 km of eastern Nevada and western Utah, between the more rapidly deforming Walker Lane and Wasatch fault zones.

We use a new analysis method, focusing on time series of cumulative strain inside triangular station subnetworks, to provide the most sensitive measurement of crustal deformation possible with the functioning GPS network. This technique reveals that the evolution of strain deviates relatively little from constant steady linear increase in strain. This finding is inconsistent with episodic translation of quasi-rigid domains, such as predicted by the active megadetachment hypothesis of *Davis et al.* [2006] and *Wernicke et al.* [2008].

The dominant signal in Nevada is a distributed shear roughly consistent with Pacific/North America relative plate motion, suggesting that stresses are transmitted through the lithosphere at least 800 km from the plate boundary. The observed active extension is consistent with earthquake focal mechanisms, distribution of seismicity, and with integrated rates estimated from earthquake geology. The Basin and Range deforms everywhere and all the time.

Acknowledgments

We obtained GPS data from the UNAVCO and SOPAC data archives. This research would not have been possible without continued support for these facilities and geodetic networks. Primary funding for this research came from NSF EarthScope award EAR-1053356 to W.C.H. and G.B. We are also grateful for the support from NSF EarthScope awards EAR-0844389, EAR-1252210, and EAR-0952166, and NASA project NNX12AK26G. We used the Generic Mapping Tools software of *Wessel and Smith* [1998] to generate Figures 1 and 4.

References

- Bar Sever, Y. E., P. M. Kroger, and J. A. Borjesson (1998), Estimating horizontal gradients of tropospheric path delay with a single GPS receiver, *J. Geophys. Res.*, *103*, 5019–5035, doi:10.1029/97JB03534.
- Bell, J. W., S. J. Caskey, A. R. Ramelli, and L. Guerrieri (2004), Pattern and rates of faulting in the central Nevada seismic belt, and paleoseismic evidence for prior belt-like behavior, *Bull. Seismol. Soc. Am.*, *94*, 1229–1254.
- Bell, J. W., F. Amelung, and C. D. Henry (2012), InSAR analysis of the 2008 Reno-Mogul earthquake swarm: Evidence for westward migration of Walker Lane style dextral faulting, *Geophys. Res. Lett.*, *39*, L18306, doi:10.1029/2012GL052795.
- Bennett, R. A., B. P. Wernicke, and J. L. Davis (1998), Continuous GPS measurements of contemporary deformation across the northern Basin and Range province, *Geophys. Res. Lett.*, *25*(4), 563–566.
- Bennett, R. A., B. P. Wernicke, N. A. Niemi, A. M. Friedrich, and J. L. Davis (2003), Contemporary strain rates in the northern Basin and Range province from GPS data, *Tectonics*, *22*(2), 1008, doi:10.1029/2001TC001355.
- Berglund, H. T., A. F. Sheehan, M. H. Murray, M. Roy, A. R. Lowry, S. R. Nerem, and F. Blume (2012), Distributed deformation across the Rio Grande Rift, Great Plains, and Colorado Plateau, *Geology*, *40*(1), 23–26, doi:10.1130/G32418.1.
- Bertiger, W., S. D. Desai, B. Haines, N. Harvey, A. W. Moore, S. Owen, and J. P. Weiss (2010), Single receiver phase ambiguity resolution with GPS data, *J. Geod.*, *84*(5), 327–337, doi:10.1007/s00190-010-0371-9.
- Blewitt, G. (1989), Carrier phase ambiguity resolution for the Global Positioning System applied to geodetic baselines up to 2000 km, *J. Geophys. Res.*, *94*(B8), 10,187–10,283, doi:10.1029/JB094iB08p10187.
- Blewitt, G., W. C. Hammond, and C. Kreemer (2009), Geodetic constraints on contemporary deformation in the northern Walker Lane: 1, Semi-permanent GPS strategy, in *Late Cenozoic Structure and Evolution of the Great Basin – Sierra Nevada Transition*, edited by J. S. Oldow and P. Cashman, pp. 1–15, Geol. Soc. Am.
- Blewitt, G., C. Kreemer, W. C. Hammond, and J. Goldfarb (2013), Terrestrial Reference Frame NA12 for crustal deformation studies in North America, *J. Geodyn.*, *72*, 11–24, doi:10.1016/j.jog.2013.08.004.
- Boehm, J., A. Niell, P. Tregoning, and H. Schuh (2006), Global mapping function (GMF): A new empirical mapping function based on numerical weather model data, *Geophys. Res. Lett.*, *33*, L07304, doi:10.1029/2005GL025546.
- Bormann, J. (2013), New insights into strain accumulation and release in the central and northern Walker Lane, Pacific-North American plate boundary, California and Nevada, USA, PhD dissertation, August, 2013, University of Nevada, Reno.
- Bormann, J., B. Surpless, S. G. Wesnousky, and M. W. Caffee (2012), Holocene earthquakes and late Pleistocene slip rate estimates on the Wassuk Range fault zone, Nevada, USA, *Bull. Seismol. Soc. Am.*, *102*(4), 1884–1891, doi:10.1785/0120110287.
- Calais, E., J. Y. Han, C. DeMets, and J. M. Nocquet (2006), Deformation of the North American plate interior from a decade of continuous GPS measurements, *J. Geophys. Res.*, *111*, B06402, doi:10.1029/2005JB004253.
- Chang, W.-L., R. B. Smith, C. M. Meertens, and R. A. Harris (2006), Contemporary deformation of the Wasatch Fault, Utah, from GPS measurements with implications for inter-seismic fault behavior and earthquake hazard: Observations and kinematic analysis, *J. Geophys. Res.*, *111*, B11405, doi:10.1029/2006JB004326.
- Davis, J. L., R. A. Bennett, and B. P. Wernicke (2003), Assessment of GPS velocity accuracy for the Basin and Range Geodetic Network (BARGEN), *Geophys. Res. Lett.*, *30*(7), 1411, doi:10.1029/2003GL016961.
- Davis, J. L., B. P. Wernicke, S. Bisnath, N. A. Niemi, and P. Elosegui (2006), Subcontinental-scale crustal velocity changes along the Pacific-North America plate boundary, *Nature*, *441*, 1131–1134.
- dePolo, C. M. (2008), Quaternary Faults in Nevada: Nevada Bureau of Mines and Geology Map 167, 1:1,000,000 scale.

- dePolo, C. M., K. D. Smith, and C. D. Henry (2011), Summary of the 2008 Wells, Nevada earthquake documentation volume, in *The 21 February 2008 Mw 6.0 Wells, Nevada Earthquake: A Compendium of Earthquake-Related Investigations Prepared by the University of Nevada, Reno, Spec. Publ.*, vol. 36, edited by C. M. dePolo and D. D. LaPointe, pp. 7–14, Nevada Bureau of Mines and Geology, Reno, Nev.
- Dixon, T. H., M. Miller, F. Farina, H. Wang, and D. Johnson (2000), Present-day motion of the Sierra Nevada block and some tectonic implications for the Basin and Range province, North American Cordillera, *Tectonics*, 19(1), 1–24, doi:10.1029/1998TC001088.
- Dokka, R. K., and C. J. Travis (1990), Role of the Eastern California Shear Zone in Accommodating Pacific-North-American Plate Motion, *Geophys. Res. Lett.*, 17(9), 1323–1326, doi:10.1029/GL017i009p01323.
- Doser, D. I. (1988), Source parameters of earthquakes in the Nevada seismic zone, 1915–1943, *J. Geophys. Res.*, 93(B12), 15,001–15,015, doi:10.1029/JB093iB12p15001.
- England, P., and D. McKenzie (1982), A thin viscous sheet model for continental deformation, *Geophys. J. R. Astron. Soc.*, 70, 295–321.
- England, P., G. A. Houseman, and L. J. Sonder (1985), Length scales for continental deformation in convergent, divergent, and strike-slip environments: Analytical and approximate solutions for a thin viscous sheet model, *J. Geophys. Res.*, 90(B5), 3551–3557, doi:10.1029/JB090iB05p03551.
- Flesch, L. M., W. E. Holt, A. J. Haines, and B. Shen-Tu (2000), Dynamics of the Pacific-North America plate boundary in the western United States, *Science*, 287, 834–836.
- Freed, A. M., R. Bürgmann, and T. Herring (2007), Far-reaching transient motions after Mojave earthquakes require broad mantle flow beneath a strong crust, *Geophys. Res. Lett.*, 34, L19302, doi:10.1029/2007GL030959.
- Gosh, A., T. W. Becker, and E. D. Humphreys (2013), Dynamics of the North American continent, *Geophys. J. Int.*, 194, 651–669, doi:10.1093/gji/ggt151.
- Gourmelen, N., and F. Amelung (2005), Post-seismic deformation in the central Nevada seismic belt detected by InSAR: Implications for Basin and Range dynamics, *Science*, 310, 1473–1476.
- Gourmelen, N., F. Amelung, F. Casu, M. Manzo, and R. Lanari (2007), Mining-related ground deformation in Crescent Valley, Nevada: Implications for sparse GPS networks, *Geophys. Res. Lett.*, 34, L09309, doi:10.1029/2007GL029427.
- Haller, K. M., M. N. Machette, R. L. Dart, and B. S. Rhea (2004), U.S. Quaternary fault and fold database released, *Eos Trans. AGU*, 85(22), 218–218, doi:10.1029/2004EO220004.
- Hammond, W. C., and W. Thatcher (2004), Contemporary tectonic deformation of the Basin and Range province, western United States: 10 years of observation with the Global Positioning System, *J. Geophys. Res.*, 109, B08403, doi:10.1029/2003JB002746.
- Hammond, W. C., C. Kreemer, and G. Blewitt (2009), Geodetic constraints on contemporary deformation in the northern Walker Lane: 3. Central Nevada seismic belt postseismic relaxation, *Late Cenozoic Structure and Evolution of the Great Basin-Sierra Nevada Transition: Geol. Soc. Am. Spec. Pap.*, 447, edited by J. S. Oldow and P. H. Cashman, pp. 33–54, doi:10.1130/2009.2447(03).
- Hammond, W. C., C. Kreemer, G. Blewitt, and H. P. Plag (2010), Effect of viscoelastic postseismic relaxation on estimates of interseismic crustal strain accumulation at Yucca Mountain, Nevada, *Geophys. Res. Lett.*, 37, L06307, doi:10.1029/2010GL042795.
- Hammond, W. C., G. Blewitt, and C. Kreemer (2011a), Block modeling of crustal deformation of the northern Walker Lane and Basin and Range from GPS velocities, *J. Geophys. Res.*, 116, B04402, doi:10.1029/2010JB007817.
- Hammond, W. C., G. Blewitt, C. Kreemer, J. R. Murray-Moraleda, and J. Svarc (2011b), Global Positioning System constraints on crustal deformation before and during the 21 February 2008 Wells, Nevada M 6.0 Earthquake, in *The 21 February 2008 Mw 6.0 Wells, Nevada Earthquake—A Compendium of Earthquake-Related Investigations Prepared by the University of Nevada, Reno, Spec. Publ.*, vol. 36, edited by C. M. dePolo and D. D. LaPointe, pp. 181–196, Nevada Bureau of Mines and Geology, Reno, Nev.
- Hammond, W. C., G. Blewitt, Z. Li, H.-P. Plag, and C. Kreemer (2012), Contemporary uplift of the Sierra Nevada, western United States, from GPS and InSAR measurements, *Geology*, 40(7), 667–670, doi:10.1130/G32968.1.
- Heidbach, O., M. Tingay, A. Barth, J. Reinecker, D. Kurfeß, and B. Müller (2009), The World Stress Map based on the database release 2008, equatorial scale 1:46,000,000, Commission for the Geological Map of the World, Paris, doi:10.1594/GFZ.WSM.Map2009.
- Hetland, E. A., and B. H. Hager (2003), Postseismic relaxation across the Central Nevada Seismic Belt, *J. Geophys. Res.*, 108(B8), 2394, doi:10.1029/2002JB002257.
- Humphreys, E. D., and D. D. Coblenz (2007), North American dynamics and western U.S. tectonics, *Rev. Geophys.*, 45, RG3001, doi:10.1029/2005RG000181.
- Jones, C. H., J. R. Unruh, and L. J. Sonder (1996), The role of gravitational potential energy in active deformation in the southwestern United States, *Nature*, 381, 37–41.
- Kent, G. M., et al. (2005), 60 k.y. record of extension across the western boundary of the Basin and Range province: Estimate of slip rates from offset shoreline terraces and a catastrophic slide beneath Lake Tahoe, *Geology*, 33(5), 356–368, doi:10.1130/G21230.1.
- Koehler, R., and S. G. Wesnousky (2011), Late Pleistocene regional extension rate derived from earthquake geology of late Quaternary faults across Great Basin, Nevada between 38.5° and 40°N latitude, *Geol. Soc. Am. Bull.*, 123, 621–650, doi:10.1130/30111.30111.
- Kreemer, C., G. Blewitt, and W. C. Hammond (2010), Evidence for an active shear zone in southern Nevada linking the Wasatch fault to the Eastern California shear zone, *Geology*, 38(5), 475–478.
- Martinez, L. J., C. M. Meertens, and R. B. Smith (1998), Rapid deformation rates along the Wasatch fault zone, Utah, from first GPS measurements with implications for earthquake hazard, *Geophys. Res. Lett.*, 25, 567–570, doi:10.1029/98GL00090.
- McClusky, S. C., S. C. Bjornstad, B. H. Hager, R. W. King, B. J. Meade, M. M. Miller, F. C. Monastero, and B. J. Souter (2001), Present Day kinematics of the Eastern California Shear zone from a geodetically constrained block model, *Geophys. Res. Lett.*, 28(17), 3369–3372, doi:10.1029/2001GL013091.
- Miller, M. M., D. J. Johnson, and T. H. Dixon (2001), Refined kinematics of the eastern California shear zone from GPS observations, 1993–1998, *J. Geophys. Res.*, 106(2), 2245–2263, doi:10.1029/2000JB900328.
- Newman, A., S. Stein, J. Weber, J. Engeln, A. Mao, and T. Dixon (1999), Slow deformation and low seismic hazard at the New Madrid seismic zone, *Science*, 284, 619–621.
- Niemi, N. A., B. P. Wernicke, A. M. Friedrich, M. Simons, R. A. Bennett, and J. L. Davis (2004), BARGEN continuous GPS data across the eastern Basin and Range province, and implications for fault system dynamics, *Geophys. J. Int.*, 159(3), 842–862.
- Oldow, J., C. L. V. Aiken, J. L. Hare, J. F. Ferguson, and R. F. Hardyman (2001), Active displacement transfer and differential block motion within the central Walker Lane, western Great Basin, *Geology*, 29(1), 19–22.
- Parsons, T., and W. Thatcher (2011), Diffuse Pacific-North American plate boundary: 1000 km of dextral shear inferred from modeling geodetic data, *Geology*, 39(10), 943–946, doi:10.1130/G32176.1.
- Patton, H. J., and G. Zandt (1991), Seismic moment tensors of western U.S. earthquakes and implications for the tectonic stress field, *J. Geophys. Res.*, 96(1111), 18,245–18,259, doi:10.1029/91JB01838.
- Payne, S. J., R. McCaffrey, R. W. King, and S. A. Kattenhorn (2012), A new interpretation of deformation rates in the Snake River Plain and adjacent Basin and Range regions based on GPS measurements, *Geophys. J. Int.*, 189(1), 101–122, doi:10.1111/j.1365-246X.2012.05370.x.
- Petersen, M. D., Y. Zeng, K. M. Haller, R. McCaffrey, W. C. Hammond, P. Bird, M. Moschetti, Z. Shen, J. Bormann, and W. Thatcher (2014), Geodesy- and geology-based slip-rate models for the Western United States (excluding California) national seismic hazard maps, *U.S. Geological Survey Open-File Report 2013-1293*, p. 80, doi:10.3133/ofr20131293.

- Pollitz, F. F. (1997), Gravitational-viscoelastic postseismic relaxation on a layered spherical Earth, *J. Geophys. Res.*, *102*, 17,921–17,941, doi:10.1029/97JB01277.
- Pollitz, F. F., P. McCrory, J. Svarc, and J. Murray (2008), Dislocation models of interseismic deformation in the western United States, *J. Geophys. Res.*, *113*, B04413, doi:10.1029/2007JB005174.
- Puskas, C. M., and R. B. Smith (2009), Intraplate deformation and microplate tectonics of the Yellowstone hot spot and surrounding western US interior, *J. Geophys. Res.*, *114*, B04410, doi:10.1029/2008JB005940.
- Puskas, C. M., R. B. Smith, C. M. Meertens, and W. L. Chang (2007), Crustal deformation of the Yellowstone-Snake River Plain volcano-tectonic system: Campaign and continuous GPS observations, 1987–2004, *J. Geophys. Res.*, *112*, B03401, doi:10.1029/2006JB0044325.
- Savage, J. C., and R. O. Burford (1973), Geodetic determination of relative plate motion in central California, *J. Geophys. Res.*, *78*(5), 832–845, doi:10.1029/JB078i005p00832.
- Savage, J. C., W. Gan, and J. L. Svarc (2001), Strain accumulation and rotation in the eastern California shear zone, *J. Geophys. Res.*, *106*, 21,995–22,007, doi:10.1029/2000JB000127.
- Scherneck, H.-G. (1991), A parameterized solid earth tide model and ocean tide loading effects for global geodetic baseline measurements, *Geophys. J. Int.*, *106*(3), 677–694, doi:10.1111/j.1365-246X.1991.tb06339.x.
- Silver, P. G., and W. E. Holt (2002), The mantle flow field beneath western North America, *Science*, *295*, 1054–1058.
- Slemmons, B., A. E. Jones, and J. I. Gimlett (1965), Catalog of Nevada earthquakes, 1852–1960, *Bull. Seismol. Soc. Am.*, *55*(2), 519–565.
- Smith, K., J. Pechmann, M. Meremonte, and K. Pankow (2011), Preliminary analysis of the M_w 6.0 Wells, Nevada, Earthquake sequence, in *The 21 February 2008 M_w 6.0 Wells, Nevada Earthquake, Spec. Publ.*, vol. 36, edited by C. dePolo and D. D. LaPointe, pp. 127–145, Nevada Bureau of Mines and Geology, Reno, Nev.
- Stein, S. (2007), New Madrid GPS: Much ado about nothing?, *Eos Trans. AGU*, *88*, 58–60, doi:10.1029/2007EO050007.
- Thatcher, W. (2009), How the continents Deform: The evidence from tectonic geodesy, *Annu. Rev. Earth Planet. Sci.*, *37*, 237–262.
- Thatcher, W., and F. Pollitz (2008), Temporal evolution of continental lithospheric strength in actively deforming regions, *GSA Today*, *18*(4/5), 4–11, doi:10.1130/GSAT01804-5A.1.
- Thatcher, W., G. R. Foulger, B. R. Julian, J. L. Svarc, E. Quilty, and G. W. Bawden (1999), Present-day deformation across the Basin and Range province, western United States, *Science*, *283*, 1714–1718.
- Wallace, R. E. (1984), Patterns and timing of late quaternary faulting in the Great Basin province and relation to some regional tectonic features, *J. Geophys. Res.*, *89*(B7), 5763–5769, doi:10.1029/JB089iB07p05763.
- Wdowinski, S., Y. Bock, J. Zhang, P. Fang, and J. Genrich (1997), Southern California Permanent GPS Geodetic Array: Spatial filtering of daily positions for estimating coseismic and postseismic displacements induced by the 1992 Landers earthquake, *J. Geophys. Res.*, *102*, 18,057–18,070, doi:10.1029/97JB01378.
- Wernicke, B. P., A. M. Friedrich, N. A. Niemi, R. A. Bennett, and J. L. Davis (2000), Dynamics of plate boundary fault systems from Basin and Range Geodetic Network (BARGEN) and Geologic Data, *GSA Today*, *10*(11), 1–7.
- Wernicke, B., J. L. Davis, N. A. Niemi, P. Luffi, and S. Bisnath (2008), Active megadetachment beneath the western United States, *J. Geophys. Res.*, *113*, B11409, doi:10.1029/2007JB005375.
- Wesnousky, S. G., A. D. Baron, R. W. Briggs, J. S. Caskey, S. J. Kumar, and L. Owen (2005), Paleoseismic transect across the northern Great Basin, *J. Geophys. Res.*, *110*, B05408, doi:10.1029/2004JB003283.
- Wesnousky, S. G., J. M. Bormann, C. Kreemer, W. C. Hammond, and J. N. Brune (2012), Neotectonics, geodesy, and seismic hazard in the northern Walker Lane of western North America: Thirty kilometers of crustal shear and no strike-slip?, *Earth Planet. Sci. Lett.*, *329–330*, 133–140, doi:10.1016/j.epsl.2012.02.018.
- Wessel, P., and W. H. F. Smith (1998), New, improved version of Generic Mapping Tools released, *Eos Trans. AGU*, *79*, 579, doi:10.1029/98EO00426.
- Williams, S. P. D. (2003), The effect of coloured noise on the uncertainties of rates estimated from geodetic time series, *J. Geod.*, *76*, 483–494.
- Zoback, M. L., and W. D. Mooney (2003), Lithospheric buoyancy and continental intraplate stresses, *Int. Geol. Rev.*, *45*, 95–116.
- Zumberge, J. F., M. B. Heflin, D. C. Jefferson, M. M. Watkins, and F. H. Webb (1997), Precise point positioning for the efficient and robust analysis of GPS data from large networks, *J. Geophys. Res.*, *102*(B3), 5005–5017, doi:10.1029/96JB03860.